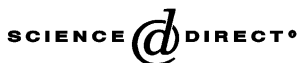
Available online at [www.sciencedirect.com](http://www.sciencedirect.com)

## Boron diffusion in silicon: the anomalies and control by point defect engineering

Lin Shao<sup>\*</sup>, Jiarui Liu, Quark Y. Chen, Wei-Kan Chu

*Department of Physics, and Texas Center for Superconductivity and Advanced Materials,  
University of Houston, Houston, TX 77004, USA*

Accepted 11 August 2003

### Abstract

The fabrication of ultra large-scale integrated (ULSI) circuits with ever shrinking feature size requires a continued reduction of diffusion lengths of dopants in Si. However, boron implants undergo an “anomalous” diffusion upon annealing, which is detrimental to the ultra-shallow junction formation. Over the last decade, boron transient diffusion has been much better understood. This implantation-induced transient-enhanced diffusion is known to be driven by the large supersaturation of self-interstitial silicon atoms emitted from the extended defects. The form and evolution of implantation-induced defects with respect to implant species, energy, dose, and annealing temperature have been systematically studied. The improved understanding has led to the development of new doping techniques, such as carbon co-implant, multiple step annealing and point defect engineering (PDE) using co-implantation of high-energy ions. In the PDE approach, high-energy ion bombardments inject vacancies near the surface region and create excessive interstitials near the end of projected range deep inside the substrate. Such manipulation of point defects can retard boron diffusion and enhance the activation of boron. The control of boron diffusion could be used to form ultra-shallow junctions for next generation Si device. In this article, we review the history and recent progress in PDE.

© 2003 Elsevier B.V. All rights reserved.

**Keywords:** Boron diffusion; Shallow junction; Point defect engineering

### 1. Introduction

The mechanism of dopant diffusion in semiconductors is a subject of considerable interest for reasons of both scientific curiosity and technological importance. One of the processing steps in the fabrication of silicon-based integrated circuits involves selective introduction of dopant atoms into the silicon substrate via ion implantation. During the subsequent annealing to remove damage and to activate dopants, redistribution of dopant exhibited diffusion behaviors much more complicated than what's predicted by the Fick's laws of diffusion. One such complication is transient diffusion, which spreads the dopant profiles several orders of magnitude larger than that under normal condition. It is generally accepted that most dopants, such as B, P, As and Sb, diffuse in silicon via fast diffusing intermediates. For example, for interstitial-mediated diffusion of B in Si, the favored pathway is through the kick-out reaction. In this reaction, self-interstitial changes place with a substitutional dopant atom to form an interstitial impurity atom that migrates for some distance before

<sup>\*</sup> Corresponding author. Tel.: +1-713-743-8259; fax: +1-713-743-8201.  
E-mail address: [lin.shao@mail.uh.edu](mailto:lin.shao@mail.uh.edu) (L. Shao).

### Nomenclature

|                       |  |
|-----------------------|--|
| $a$                   | Si lattice constant  |
| $B_C$                 | immobile B clusters  |
| $B_i$                 | interstitial B   |
| $B_s$                 | substitutional B   |
| $C_I$                 | concentration of Si interstitials  |
| $C_{IT}$              | concentration of interstitial-trap complex                                   |
| $\langle C_I \rangle$ | time-averaged concentration of Si interstitials                              |
| $C_I^*$               | equilibrium concentration of Si interstitials                                |
| $C_i$                 | interstitial carbon atoms in silicon   |
| $C_s$                 | substitutional carbon atoms in silicon                                       |
| $C_T$                 | concentration of traps   |
| $C_V$                 | concentration of Si vacancies  |
| $C_V^*$               | equilibrium concentration of Si vacancies                                    |
| $C_X$                 | concentration of point defects X   |
| $D_B$                 | diffusivity of B in silicon  |
| $D_B^*$               | diffusivity of B in silicon under equilibrium condition                      |
| $\langle D_B \rangle$ | time-averaged diffusivity of B   |
| $D_I$                 | diffusivity of silicon self-interstitials                                    |
| $D_{(i)}$             | interstitial-mediated components of diffusion for a species in Si            |
| $D_I^{\text{eff}}$    | effective diffusivity of Si self-interstitials                               |
| $D_m$                 | diffusivity of migrating species   |
| $D_{\text{self}}$     | diffusivity of Si self-diffusion in Si                                       |
| $D_V$                 | diffusivity of Si vacancies in Si  |
| $D_{(v)}$             | vacancy-mediated components of diffusion for a species in silicon            |
| $D_X$                 | diffusion coefficients of point defect or impurity X                         |
| $E_b$                 | binding energy of silicon interstitial in an interstitial type defect        |
| $E_b^c(n)$            | binding energy of vacancy clusters in silicon with cluster size = $n$        |
| $E_{\text{diss}}$     | dissociation energy of clusters  |
| $E_{\text{fc}}$       | formation energy of a specific interstitial clusters in Si                   |
| $E_m$                 | migration energy of Si interstitial  |
| $f_{I,V}$             | correlation factors for the corresponding diffusion mechanisms               |
| $g(g^*)$              | reaction probability for $X_s \rightarrow X_m$ (under equilibrium condition) |
| $g_X$                 | a geometric factor depending on the crystal structure                        |
| $H_X^f$               | enthalpy of formation of point defect X, while $X = I$ or $V$                |
| $H_X^m$               | enthalpy of migration of point defect X, while $X = I$ or $V$                |
| $I$                   | self-interstitials   |
| $IT$                  | interstitial-trap complexes  |
| $k_B$                 | Boltzmann's constant   |
| $k(k')$               | reaction constant in forward (reverse) direction                             |
| $N_0$                 | number of available lattice sites in the crystal                             |
| $n_i$                 | intrinsic carrier concentration  |
| $Q_{\text{self}}$     | activation energy of self-diffusion of silicon                               |
| $r(r^*)$              | reaction probability for $X_m \rightarrow X_s$ (under equilibrium condition) |
| $S_X^f$               | formation entropy of point defect X  |

|         |  |
|---------|--|
| $S_X^m$ | migration entropy of point defect X            |
| $T$     | temperature                                    |
| $T$     | bulk trap for defects                          |
| $\nu$   | attempt frequency for diffusion                |
| $V$     | vacancies                                      |
| $X_i$   | interstitial impurity atoms                    |
| $XI$    | a complex between impurity and Si interstitial |
| $X_m$   | migrating impurity atoms                       |
| $X_s$   | substitutional impurity atoms                  |
| $XV$    | a complex between impurity and Si vacancy      |

*Greek letters*

|            |  |
|------------|--|
| $\theta_X$ | number of degree of freedom for the defect X on a lattice site |
| $\lambda$  | migration distance of an impurity                              |

recombination with a vacancy at a substitutional site. These interstitial dopants have migration energies less than those of self-interstitials. Such ‘anomalous’ diffusion proceeds at an enhanced rate that depends on silicon self-interstitial concentration at a given depth. For boron in silicon, ‘anomalous’ diffusion rates at early stage of annealing are observed, which are several orders of magnitude higher than the ‘normal’ diffusion rates observed under longer annealing duration. This phenomenon has been named transient-enhanced diffusion (TED) in the vast majority of literature.

Driven by the technological needs, much effort was spent over the last 30 years to understand the enhanced diffusion process, and to find a way to counteract its undesirable effects. However, without full understanding of the mechanism, it is very difficult to control the diffusion by any method other than trial and error. One counteracting phenomenon, which was observed and confirmed early on, is suppressed TED with carbon co-implantation. For such a suppression, it requires a very high concentration of carbon ( $\sim 1 \times 10^{19} \text{ cm}^{-3}$ ) which, when implemented, may adversely affect the eventual device performance. More recently, another promising TED suppression method was observed via co-implantation with MeV Si ions. Since momentum transferred to target atoms is usually in the forward direction, it makes the distribution of interstitials slightly deeper than vacancies. Hence, this produces a vacancy rich region close to the surface and an interstitial rich region near the end of the range of the MeV projectiles. It has been demonstrated by many authors that the TED reduction is due to undersaturation of interstitials in the vacancy rich region. Common interests in these efforts were to understand and manipulate the point defects, or point defect engineering (PDE).

The main purpose of this review is to: (1) document the point defect generation and diffusion under thermal equilibrium condition, and their interplay with dopant diffusion; (2) review the understanding on TED for boron in silicon and various other defect-instigated diffusion phenomena; (3) discuss a recently discovered enhanced diffusion phenomenon, named boride enhanced diffusion; (4) review on the efforts to control boron diffusion. Reducing boron diffusion below its normal rate has been accomplished by point defect engineering (PDE) with co-implantation of high-energy ions. Boron junctions less than 10 nm deep can be formed using PDE. The findings not only have significant importance for next generation complementary metal-oxide-semiconductor (CMOS) device fabrication, but also give a deeper insight into the dopant–defect interaction such as interstitial–vacancy recombination, trapping and diffusion.

In this article, fundamental studies on intrinsic point defects and self-diffusion are discussed in Sections 2 and 3. We then review the studies on the conventional dopant diffusion mechanisms and

recently updated knowledge on the enhanced diffusion of boron in [Section 4](#). Techniques of defect engineering and its applications on shallow junction formation are reviewed in [Section 5](#). Other methods such as co-implantation of carbon or fluorine on the boron TED reduction are given in [Section 6](#). Finally, we proceed to a specific discussion on the vacancy and vacancy clusters in [Section 7](#) before drawing a conclusion.

## 2. Intrinsic point defects in single crystal silicon

A quantitative understanding of intrinsic point defects in Si is essential to the understanding of transport processes of dopants in Si since point defects are the primary mediators of dopant diffusion. A general expression for the equilibrium concentration  $C_X$  of point defects X, where X could be I (interstitials), or V (vacancies), is given by [1].

$$C_X = N_0 \theta_X \exp\left(\frac{S_X^f}{k_B}\right) \exp\left(\frac{-H_X^f}{k_B T}\right), \quad (2.1)$$

where  $k_B$  is the Boltzmann constant,  $N_0$  the number of available lattice sites per unit volume in the crystal,  $H_X^f$  the enthalpy of formation,  $S_X^f$  the entropy of formation and  $\theta_X$  the number of degree of freedom for the defect X on a lattice site.

The diffusion coefficients  $D_X$  can be written as

$$D_X = g_X a^2 \nu_X \exp\left(\frac{S_X^m}{k_B}\right) \exp\left(\frac{-H_X^m}{k_B T}\right), \quad (2.2)$$

where  $g_X$  is a geometric factor depending on the crystal structure and on the microscopic jump geometry of the diffusion process ( $g_X = 1/4$  for the Si interstitials, or  $g_X = 1/8$  for the vacancies).  $a$  (0.54 nm) is the Si lattice constant and  $\nu_X$  is the attempt frequency, and  $S_X^m$  and  $H_X^m$  are the entropy and the enthalpy of migration, respectively.

Point defects cannot be observed directly by most microscopic means and, as a consequence, their properties and influences are mostly determined via indirect methods, e.g. studying foreign-atom diffusion when point defects are involved in the diffusion process. This, however, needs the concentration of these point defects to deviate significantly from their equilibrium values. Such non-equilibrium conditions can be realized by electron irradiation, implantation, oxidation or nitridation of Si [2]. For 40 years, there have been two major types of experiments performed in Si. The first involves the diffusion of groups III or V elements, while the second involves the diffusion of metallic atoms. Basically, on lattice scale, there are four types of diffusion mechanisms in Si, summarized as the following:



where  $X_s$  and  $X_i$  are substitutional and interstitial impurity atoms, respectively. The defects XI and XV represent a complex, or a coupling between impurity atoms and intrinsic defects. The first and

second reactions are called the interstitial mechanism and kick-out mechanism, respectively. The third and fourth are called the vacancy mechanism and the Frank–Turnbull (or dissociative) mechanism, respectively.

Metal atoms in Si can diffuse either via the kick-out mechanism (2.4) that involves self-interstitials, or via Frank–Turnbull mechanism (2.6) that involves vacancies. For a interstitial or kick-out mechanism, a substitutional impurity becomes an interstitial after being kicked out by an approaching silicon interstitial, and migrate until it kicks in or is trapped. Therefore, the probabilities for  $X_s \rightarrow X_m$ , where the migrating species  $X_m$  is XI for reaction (2.3) and  $X_i$  for reaction (2.4), is proportional to silicon interstitial concentration  $C_i$  by  $g = g^* C_i / C_i^*$ . The quantity  $C_i^*$  refers to the equilibrium concentration of interstitials. For vacancy assisted reaction (2.5), the quantity  $g$  is proportional to vacancy concentration by  $g = g^* C_v / C_v^*$ . For Frank–Turnbull mechanism (2.6),  $g$  remains a quantity at equilibrium condition. But the quantity  $r$ , the probability of  $X_m \rightarrow X_s$ , is proportional to vacancy concentration  $C_v$  by  $r = r^* C_v / C_v^*$ . The general transport equations for all four reactions can be described by

$$\frac{\partial C_m}{\partial t} = D_m \nabla^2 C_m - r C_m + g C_s, \quad (2.7)$$

$$\frac{\partial C_s}{\partial t} = D_s \nabla^2 C_s + r C_m - g C_s \quad (2.8)$$

Analysis of the diffusion of metal species such as gold or platinum at high temperature would give an estimate of the equilibrium concentration of interstitials since they diffuse in Si mainly via a kick-out mechanism. On the contrary, analysis of the diffusion of Sb would give an estimate of the equilibrium concentration of vacancy since Sb diffusion in Si is primarily driven by vacancies.

Studies on the thermodynamic and transport properties of interstitial and vacancy in Si has been reviewed by Fahey et al. [2] and others [3,4]. In this article, we intend to document the updated results from different research groups and compare their experimental results with theoretical calculations. Such updated comparisons can help give an insight into the complexity and difficulty of the diffusion problem.

Table 1 and Fig. 1 summarize the model-fitted experimental results for self-interstitial concentrations [5–21]. Since defect supersaturation associated with the metal diffusion can be simulated by coupled diffusion, the success of an experiment heavily relies on the good control of the starts and ends of diffusion. It is necessary that the defects have reached equilibrium

Table 1  
Silicon self-interstitial concentration parameters determined by various experimental methods

| Formation enthalpy (eV) | Migration enthalpy (eV) | Remark  |
|-------------------------|-------------------------|---|
| 3.84                    | 0.97                    | Au and Pt diffusion (Zimmermann and Ryssel [5])     |
| 4.4                     | 0.4                     | Swirl defects (Tan and Gósele [8])                  |
| 3.8                     |                         | Au and Pt diffusion (Morehead [9])                  |
| 3.26                    | 1.58                    | OED (Kump and Dutton [14])                          |
| 3.18                    | $1.77 \pm 0.12$         | Zn diffusion (Bracht et al. [6])                    |
|                         | 1.86                    | Oxygen diffusion (Wijaranakula [10])                |
| 2.8                     |                         | Internal friction measurements (Seeger et al. [13]) |
| 2.5                     |                         | Post-implant annealing (Jäger et al., [15])         |
| 2.36                    | 2.44                    | Au and P diffusion (Bronner and Plummer [16])       |
| 1.58                    | 3.22                    | Rapid optical Au metal diffusion (Boit et al. [17]) |
| 0.7                     | 4.0                     | Oxidation stacking faults (Taniguchi et al. [12])   |
| 0.4                     |                         | Oxygen stacking fault growth (Wada et al. [11])     |

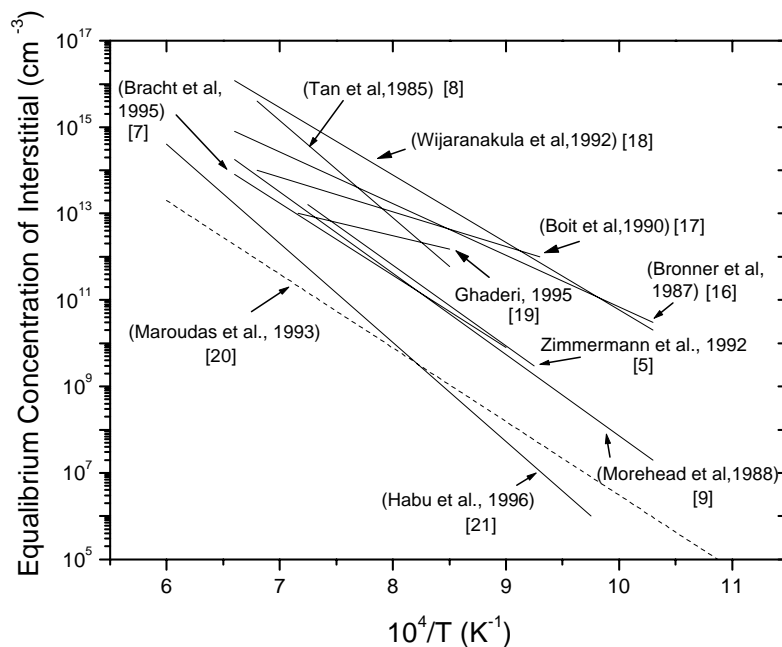


Fig. 1. Equilibrium concentration of interstitial defects in silicon. Solid lines are determined from diffusion experiments, while dash line is theoretical data.

concentrations at the beginning of the metal and dopant diffusion. For this purpose, a preannealing for 6 weeks has been performed, for example, in Zimmermann and Ryssel's Pt diffusion experiment [5]. To further avoid defect change during cooling to room temperature in the air, very elaborate experiment has been performed by Bracht et al. [6,7], where Zn is sealed in a quartz bulb inside the outer ampoule. Once thermal equilibrium is established by preannealing, the quartz bulb was broken and Zn diffusion in Si started. The ampoule was mounted in a vertical furnace and diffusion was terminated by plunging the ampoule into ethylene glycol at room temperature. The parameters of the intrinsic point defects were determined by fitting the measured diffusion profiles with coupled diffusion equation. Values obtained from Bracht's experiment seem to be by far the most accurate one and most widely referred to by the community. Equilibrium self-interstitial concentration  $C_I^*$  ( $H_I^f = 3.18$  eV) from Zn diffusion experiment [7] has a good agreement with studies on the Au and Pt diffusion experiments by Zimmermann and Ryssel ( $H_I^f = 3.8$  eV) [5], and by Morehead ( $H_I^f = 3.8$  eV) [9]. But still, most metal in-diffusion experiments lead to lower equilibrium concentration and higher diffusivity value for interstitials, when compared with other methods, such as oxidation-enhanced or oxidation-retarded diffusion experiments by Wijaranakula [10] ( $H_I^f = 2.9$  eV for I), oxygen precipitation and oxygen stacking fault growth by Wada et al. [11] ( $H_I^f = 0.4$  eV for I), oxidation stacking faults by Taniguchi et al. [12] ( $H_I^f = 0.8$  eV for I), and internal friction measurements by Seeger et al. [13] ( $H_I^f = 2.8$  eV for I).

Table 2 and Fig. 2(a) summarize the experimental results for vacancies in Si [7,8,18,21–26]. The  $C_V^*$  values extracted from Zn diffusion experiments [7] also fall within the ballpark with the data of Tan and Gösele from Au diffusion experiments [8]. It also agrees with the Pt diffusion experiments from Zimmermann [4] within the error bar. The  $C_V^*$  values extracted by Habu and Tomiura [21] and Wijaranakula [18], through modeling of crystal growth, however, deviate greatly from the other authors. The discrepancy, as discussed in a review by Zimmermann [4], is attributed to the unreliable simulation of point defect distribution during the growth and cooling of

Table 2  
Experimental equilibrium silicon vacancy concentration from the literature

| Prefactor ( $\text{cm}^{-3}$ ) | Formation enthalpy (eV) | Migration enthalpy (eV) | Remark  |
|--------------------------------|-------------------------|-------------------------|---|
| $10^{25}\text{--}10^{27}$      | 1.1                     |                         | Model fitting (Park and Law [24])               |
|                                | 2.0                     | 1.8                     | Zn diffusion (Bracht et al. [7])                |
|                                | 2.0                     | 2.0                     | Au and Pt diffusion (Zimmermann and Ryssel [5]) |
|                                | 2.6                     |                         | Positron annihilation (Van Vechten [23])        |
|                                | 2.7                     |                         | Model fitting (Mathiot and Pfister [25])        |
|                                | 3.4–3.8                 |                         | Positron annihilation (Dannefaer et al. [22])   |

the crystals, since defect reaction and complex formation have not been understood well for the crystal growth.

Estimates of vacancy concentrations can also be obtained by positron annihilation, electron paramagnetic resonance (EPR), and deep-level transient spectroscopy (DLTS). Fig. 2(b) includes the results from positron annihilation studied by Dannefaer et al. [22] and Van Vechten [23]. The values obtained from positron annihilation studies are much lower than that from metal diffusion experiments. Positron annihilation has emerged as an important tool that provides microscopic information on the vacancy defects, which capture the positron and annihilate it through a localized electron. Positron annihilation experiments in the past have observed different lifetimes of positrons for mono-vacancies and di-vacancies, yet the assignment of lifetime is still controversial. In Van Vechten's studies [23], a vacancy enthalpy of formation,  $H_V^f = 2.4 \text{ eV}$ , is extracted by assuming a simultaneous contribution of mono- and di-vacancies to the mean positron lifetime, while the same data yield a value of  $H_V^f = 3.6 \text{ eV}$  [22] by assuming a sole contribution from the mono-vacancies only.

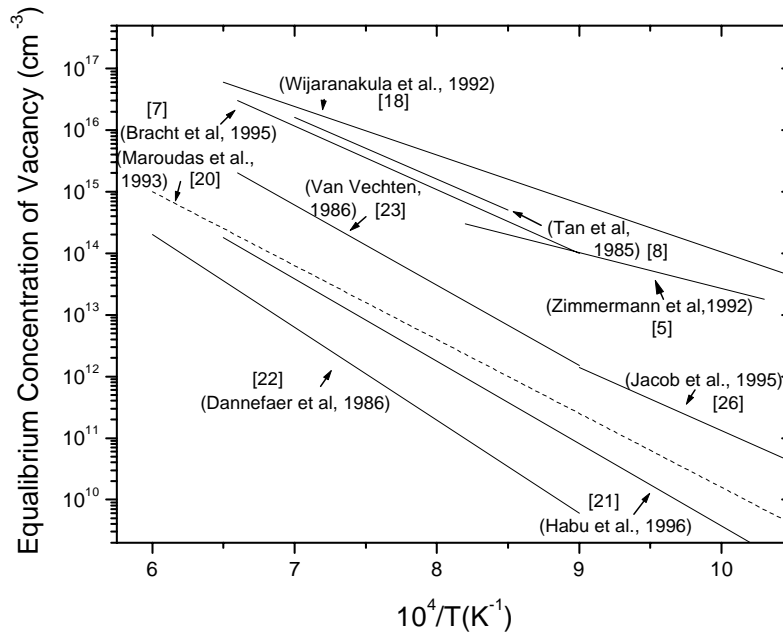


Fig. 2. Equilibrium concentration of vacancies in silicon. Solid lines are determined from diffusion experiments, while dash line is theoretical data.



Atomic-scale calculation using classical or quantum mechanical potential can offer a significant insight into the problem. With fast improvements in computational power, the accuracies in theoretical approach have improved significantly, usually within ca.  $\pm 0.2$  eV. As a consequence, direct determinations of thermodynamic parameters describing defects in various possible configurations and charge states also become feasible. For example, it has been shown that the self-interstitial has a negative-U behavior with the +2 charge state having a lower energy of formation in comparison to that of the neutral charge state [27–29]. Also shown is that self-interstitials have a strongly rebounded configuration (split) in which two Si atoms sharing one single lattice site displace along the [110] and [0 0 1] directions [30,31]. More details on split can be found in a review by de Souza and Narayanan [3]. Various methods of computation for the free energies of formation and migration have been discussed by Ungar et al. [32] and by de Souza and Narayanan [3]. Results from most of the theoretical calculations available to date are summarized in Table 3 [20,28,29,32–48].

The calculated activation energies for interstitial-mediated self-diffusion, which are the sum of the energies of formation and migration, are in the range of 4–5 eV, in agreement with Bracht's metal diffusion data ( $H_I^f + H_I^m = 4.95$  eV). However, other theoretical approaches yield interstitials energy of formation in the range of 3.4–5.0 eV, which is larger than the energy of formation (1.2–3.2 eV) from metal diffusion experiments. The reason for this discrepancy, so far, is still unknown.

As for the vacancy, the results from theoretical calculations and experiments are in agreement. Calculated energies of formation for vacancies are given in Table 4. The values, calculated using Stillinger–Weber potential and Car–Parinello techniques have been found to be less than 3 eV, which is close to the value of 2.0 eV from Zn diffusion experiment and 2.6 eV from positron lifetime measurements and 2.7 eV from the model fitting. Generally, the energy of formation for vacancies is lower than that of interstitials. This trend holds for most theoretical approaches. Obtained energy of migration for vacancies, in the range of 0.3–1.5 eV, is consistent with the experimental results by Watkins [49].

Table 3

Formation, migration and activation energy of the interstitials from various theoretical calculations

| Formation enthalpy for tetra (eV) | Formation enthalpy for hex (eV) | Migration enthalpy (eV) | Activation energy (eV) | Remark   |
|-----------------------------------|---------------------------------|-------------------------|------------------------|--|
| 3.42                              | 4.58                            | 1.05 (T–T via hex)      | 4.5                    | Tersoff potential (Ungar et al. [32])                |
| 4.84                              | 6.58                            | 1.2                     | 4.84                   | Stillinger–Weber potential (Maroudas and Brown [20]) |
| 4.95                              | 6.54                            |                         |                        | Stillinger–Weber potential (Batra et al. [33])       |
| 3.9                               | 3.9                             | 0.7(kick-out)           | 4.6                    | Ackland (de Souza and Amaratunga [34])               |
| 4.81                              | 7.07                            |                         | 4.9                    | Embedded-atom method (Baskes et al. [35])            |
| 4.7                               | 5.4                             |                         |                        | Empirical tight-binding (Rasband et al. [29])        |
| 4.42                              | 5.13                            |                         |                        | Empirical tight-binding (Kwon et al. [36])           |
| 4.41                              | 5.93                            |                         |                        | Tight-binding molecular-dynamics (Wang et al. [37])  |
| 4.7                               | 4.4                             | 1.2 ( $I^{2+}$ )        |                        | Greens function (Kelly and Car [28])                 |
| 4.7 ( $I^{2+}$ ) $\pm$ 0.4        |                                 | 0.4 $\pm$ 0.4           |                        | Greens function (Baraff and Schluter [38])           |
| 4.0 ( $I^{2+}$ )                  |                                 | 1.2                     |                        | Supercell (Bar-Yam and Joannopoulos [39])            |
| 4.3, 3.6 ( $I^{2+}$ )             |                                 |                         |                        | Supercell (Antonelli and Bernholc [40])              |
| 3.6                               |                                 | 0.4                     | 4                      | Supercell (Nichols et al. [41])                      |
| 4.95                              |                                 |                         |                        | Empirical tight-binding (Mercer and Chou [42])       |
| 4.84                              | 6.58                            | 0.9                     |                        | Stillinger–Weber potential (Gilmer et al. [43])      |
| 4.95                              |                                 |                         |                        | Stillinger–Weber potential (Schober [44])            |
| 4.39                              | 4.93                            | 1.37                    |                        | Tight-binding (Tang et al. [45])                     |
|                                   |                                 |                         | 4.79                   | Tersoff potential (Nishihira and Motooka [46])       |

Data before 1996 was taken from a review by de Souza et al.



Table 4  
Formation, migration and activation energies of the vacancy

| Formation enthalpy for mono-vacancy (eV) | Formation enthalpy for di-vacancy (eV) | Migration enthalpy (eV) | Activation energy (eV) | Remark   |
|--|--|-------------------------|------------------------|--|
| 3.97                                     |  | 0.1                     | 4.07                   | Tight-binding (Tang et al. [45])                     |
| 3.7                                      | 5.56                                   | 1.5–1.44                | 4.5–4.9                | Tersoff potential (Ungar et al. [32])                |
| 2.66                                     |  | 0.43                    | 3.09                   | Stillinger–Weber potential (Maroudas and Brown [20]) |
| 3.9                                      | 3.45                                   |                         |                        | Ackland (de Souza and Amaratunga [34])               |
| 3.19                                     | 6.0                                    |                         |                        | Embedded-atom method (Baskes et al. [35])            |
| 3.15                                     | 2.9                                    | 0.35                    | 3.56                   | Empirical tight-binding (Rasband et al. [29])        |
| 3.93                                     |  |                         |                        | Empirical tight-binding (Kwon et al. [36])           |
| 4.12                                     |  |                         |                        | Tight-binding (Wang et al. [37])                     |
| 3.8                                      |  |                         | 4.2                    | Greens function (Kelly and Car [28])                 |
| 3.6                                      |  |                         |                        | Supercell (Bar-Yam and Joannopoulos [39])            |
| 4.4                                      |  |                         |                        | Supercell (Antonelli and Bernholc [40])              |
| 3.5                                      |  | 0.3                     | 3.8                    | Supercell (Nichols et al. [41])                      |
| 3.76                                     |  |                         |                        | Empirical tight-binding (Mercer and Chou [42])       |
| 2.64                                     |  | 0.43                    | 3.07                   | Stillinger–Weber potential (Gilmer et al. [43])      |
| 4.1                                      |  | 0.3                     | 4.4                    | Car–Parinello (Car et al. [47])                      |
| 2.8                                      |  |                         |                        | Car–Parinello (Virkkunen et al. [48])                |

Data before 1996 was taken from a review by de Souza et al.

### 3. Diffusion coefficients and self-diffusion in silicon

Since the condition of the Si substrate such as concentrations of oxygen and carbon impurities can greatly influence the results, it is not surprising that certain discrepancies do exist. For interstitials, the trapping process can be annihilating traps with vacancy type defects by  $I + T \rightarrow 0$  or non-annihilating traps with carbon or other impurities by  $I + T \leftrightarrow IT$ , where T represents trapping center in Si. With combined contributions from those two trapping, no simple analytic solution is possible.

The basic equations of  $I + T \leftrightarrow IT$  are expressed as

$$\frac{\partial C_I}{\partial t} = \frac{D_I \partial^2 C_I}{\partial x^2} - k C_I C_T + k' C_{IT}, \quad (3.1)$$

$$\frac{\partial C_{IT}}{\partial t} = k C_I C_T - k' C_{IT}, \quad (3.2)$$

where  $k$  is the reaction constant in association with the trapping process in the forward direction and  $k'$  is that for the reverse reacting due to dissociation.  $k$  can be simply written in terms of effective capture radius  $r$  by  $k = 4\pi r D_I$ , where  $D_I$  is the diffusivity of Si interstitials. The average value of the diffusion coefficients of defect I in both types of configuration, free or trapped, usually has

$$D_I^{\text{eff}} = \frac{D_I C_I}{C_I + C_{IT}}. \quad (3.3)$$

Physically, this can be understood that defect I spend a fraction of  $C_I/(C_I + C_{IT})$  of its time as a freely moving defect and  $C_{IT}/(C_I + C_{IT})$  of its time attached to a trapping center T [2]. As a result,

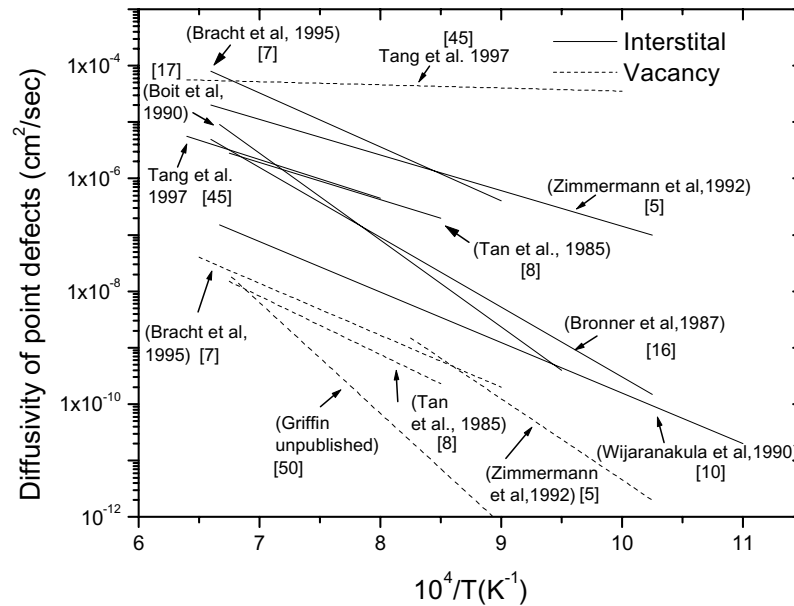


Fig. 3. Temperature dependence of the diffusivity of interstitials and vacancies, determined from various groups.

the effective diffusion coefficient can be strongly reduced when  $C_{IT} \gg C_I$ . In a similar manner, the impurities such as oxygen and carbon can retard the diffusion of vacancy defects.

The diffusion coefficients of the point defects determined from the model-fitted experiments are summarized in Fig. 3 [5,8,10,17,45,50]. Compared with the scattered data for interstitial diffusivities, vacancy diffusivity from diffusion experiments by Tan and Gösele [8], Zimmermann and Ryssel [5] and by Bracht et al. [7] are consistent with each other. However, their experimental data are four to seven order magnitude lower than the value obtained from atomic theory by Tang et al. [45]. This large discrepancy between diffusion experiment and from atomic theory cannot be explained solely by the trapping of vacancies with oxygen [51].

It is worthwhile to point out that the diffusivity of vacancies is around two orders of magnitude lower than that of interstitials. Also, many experiments found that  $C_V^* > C_I^*$  at high-temperature region, e.g. near the melting point of Si [7,52]. This, however, does not mean that vacancies are only remnant defects after V–I recombination. Due to a barrier to V–I recombination, Hu suggested that excess interstitials and vacancies did not annihilate completely and might agglomerate separately into interstitial type and vacancy type defects [53].

Silicon isotope has been used to study silicon self-diffusion over a wide range of temperatures [54–58]. These early studies were limited by the short lifetime of the radioactive tracer  $^{31}\text{Si}$ . The development of epitaxial growth technique, such as chemical vapor deposition, makes possible the study with isotopically enriched  $^{28}\text{Si}$  or  $^{30}\text{Si}$ . Taking into account all possible contributions to self-diffusion [59], one may write the diffusivity of silicon as

$$D_{\text{self}} = f_I C_I^* D_I + f_V C_V^* D_V + D_{\text{exchange}}. \quad (3.4)$$

The first two terms represent the self-interstitial and the vacancy contributions to the self-diffusion, where  $C_{I,V}^*$  and  $D_{I,V}$  are the equilibrium concentrations and the diffusion coefficients of I or V. The last item accounts for a direct exchange of adjacent lattice atoms. The contribution of

direct exchange usually is not considered, since calculations have shown that it does not play a role in Si self-diffusion [30,59,60].  $f_I$  and  $f_V$  are the correlation factors for the corresponding diffusion mechanisms. These correlation factors have been calculated by Compaan and Haven to be  $f_V = 0.5$  [61] and  $f_I = 0.73$  [62].

Almost all self-diffusion studies show a good fit to an Arrhenius form of temperature dependence with

$$D_{\text{self}} = D_{\text{self}}^0 \exp \left[ -\frac{Q_{\text{self}}}{k_B T} \right], \quad (3.5)$$

where  $Q_{\text{self}}$  is the activation energy of self-diffusion ( $\sim 4.7$  eV), which is approximately 1 eV greater than that of the dopant diffusion [63].

Experimentally, it is found that  $Q_{\text{self}} = 4.65$  eV [64,65] for temperatures lower than 1200 °C, whereas  $Q_{\text{self}} = 5.13$  eV for high temperature between 1100 and 1300 °C [55]. This characteristic temperature dependence of  $Q_{\text{self}}$  indicates that the mechanisms of Si self-diffusion are different at different temperature regions. However, Bracht et al. showed that temperature dependence of the self-diffusion coefficients can be described over seven orders of magnitude with a single enthalpy of diffusion of  $Q_{\text{self}} = 4.75$  eV for a wide range of temperatures between 850 and 1400 °C [57]. This single enthalpy implicates only one dominating mechanism in the Si self-diffusion. Elemental metal diffusion experiments [7,8,66] suggest that self-interstitials do indeed dominate the self-diffusion. First-principle calculations of self-diffusion constants in silicon also support this conclusion [30].

Ural et al. [58], extended the self-diffusion experiment to the temperature range 800–900 °C, using isotope heterostructures. By comparing P, Sb, and self-diffusion under various non-equilibrium conditions, they determined that the interstitial-mediated fraction of self-diffusion was confined between 0.50 and 0.62 for temperatures from 800 to 1100 °C. They concluded that both interstitial and vacancy mechanisms were responsible for the self-diffusion. This result is in contrast to the experiment of Bracht et al. [57]. The discrepancy still remains to be bridged.

#### 4. Dopant diffusion and transient-enhanced diffusion (TED) of B in silicon

The enhanced diffusion of dopants was first recognized more than 20 years ago [67]. This behavior has been verified and investigated extensively in the past decade [68–83].

Let  $g^*$  be the reaction probability for  $X_s$  (substitutional)  $\rightarrow X_m$  (migrating) and  $r^*$  the probability for  $X_m \rightarrow X_s$  under equilibrium conditions. The generation rate  $g$  and the migration length  $\lambda$  under non-equilibrium conditions can deviate from equilibrium values [74,75], as shown in Table 5. By introducing a parameter  $f_I$  to describe the fraction of diffusion via I-type mediation under equilibrium

Table 5

The defect generation rate and migration length for four different diffusion reactions [74]

| Dominant reaction                | Generation rate, $g$    | Migration length, $\lambda$                 |
|----------------------------------|-------------------------|---|
| $X_s + I \rightleftharpoons XI$  | $g_{X_i}^* C_I / C_I^*$ | $(D_{X_i} / r_{X_i}^*)^{1/2}$               |
| $X_s + I \rightleftharpoons X_i$ | $g_{X_i}^* C_I / C_I^*$ | $(D_{X_i} / r_{X_i}^*)^{1/2}$               |
| $X_s + V \rightleftharpoons XV$  | $g_{X_i}^* C_V / C_V^*$ | $(D_{X_i} / r_{X_i}^*)^{1/2}$               |
| $X_s + X_i \rightleftharpoons V$ | $g_{X_i}^*$             | $(D_{X_i} / (r_{X_i}^* C_V / C_V^*))^{1/2}$ |

conditions, the generation rate (kick-out frequency) for  $X_s \rightarrow X_m$  can be shown to be

$$g = g^* \left[ (1 - f_I) \frac{C_V}{C_V^*} + f_I \frac{C_I}{C_I^*} \right]. \quad (4.1)$$

For long diffusion time  $t \gg 1/g$ , the boron diffusion can be described using Fick's law with an average diffusivity

$$D = \lambda^2 g. \quad (4.2)$$

A method to extract  $g$  and  $\lambda$  from the spreading of an initial delta-doped B spike has been developed by Cowern et al. [74,75]. The changes of  $g$  and  $\lambda$  under perturbation of different type defects can help determinate the diffusion mechanism. For B–Si system, it has been shown that  $g$  is proportional to  $C_I/C_I^*$ , but  $\lambda$  is independent of  $C_I/C_I^*$ , which shows that boron diffuses via a kick-out diffusion mechanism with  $f_I \approx 1$  [74,75].

Thus, Eq. (4.2) is simplified into

$$D_B \approx D_B^* \frac{C_I}{C_I^*}. \quad (4.3)$$

It is generally believed that the silicon self-interstitials emitted from the ion implantation damages interact with the boron atoms to form B–Si pairs which diffuse very fast until they are trapped or dissociated. Enhancement of boron diffusion can go up to  $10^7$  times the normal diffusion rate during post-implant annealing. Furthermore, it has been shown that the lower the temperature, the larger  $\lambda$  becomes and the further B atoms migrate before returning to a substitutional site. The temperature dependence of  $g$  and  $\lambda$  during inert-ambient diffusion  $C_I/C_I^* \approx 1$  and during oxidizing-ambient diffusion is shown in Fig. 4. The expression of  $\lambda$  takes the form  $\lambda = \lambda_0 \exp(-E_\lambda/kT)$ , where  $E_\lambda = -0.4 \pm 0.2$  eV [75].

Observation of transient-enhanced diffusion of boron, its mechanism, and experimental results have been reviewed recently by Jain et al. [84]. In this section, we will discuss several important aspects of the TED, then touch upon boron enhanced diffusion before we get into the key topic of our review, namely point defect engineering.

#### 4.1. Intrinsic transient-enhanced diffusion (TED)

For light ions and low doses, ion implantation produces Frenkel pairs of vacancies and interstitials. The diffusing interstitials may encounter and kick-out substitutional boron atoms at the first moment of annealing, leading to ultra-fast boron enhanced diffusion. Interstitials and vacancies will annihilate each other, or migrate to the surface, or agglomerate to form small defect clusters, but those clusters may not be visible even in transmission electron microscopy [85]. Only when ion implantation dosage is high enough, rod-like extended defects appear. These defects, called  $\{3\ 1\ 1\}$  defects, precipitate on the  $\{3\ 1\ 1\}$  planes, along  $\langle 1\ 0\ 0 \rangle$  directions [82]. With low implantation dosage and hence low damage, the intrinsic TED is driven by the emitted interstitials from small clusters, while  $\{3\ 1\ 1\}$  defects contribute to TED with higher dose implantation [85].

#### 4.2. Annealing of small clusters

Ostwald ripening, a theory developed some 40 years ago, is a mechanism dominating the thermal evolution of small clusters, in which the interstitials diffuse from defect with low

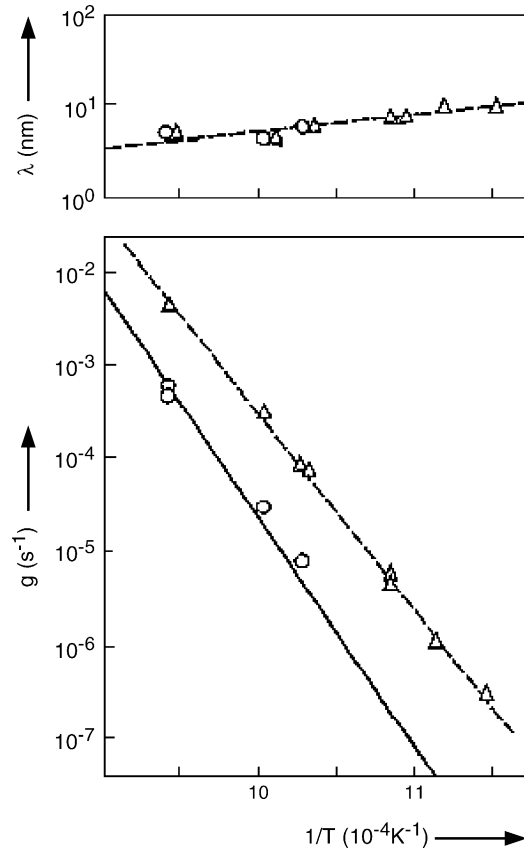


Fig. 4. Arrhenius plot of  $g$  and  $\lambda$  in the temperature range 600–800 °C. Circles indicate nitrogen ambient diffusion condition, and triangles indicate dry oxygen ambient (from [75]).

dissociation energy to form more stable defects with others [86]. Let  $N_n$  represents the numbers of cluster of size  $n$ . The evolution of  $N_n$  under Ostwald ripening can be expressed as [77]:

$$\frac{dN_n}{dt} = F_{n-1}N_{n-1} - F_nN_n - R_nN_n + R_{n+1}N_{n+1}, \quad (4.4)$$

where

$$F_n = 4\pi r_n D_I C_I, \quad (4.5)$$

$$R_n = R_{n_0} \exp\left[-\frac{E_{\text{diss}}(n)}{k_B T}\right], \quad (4.6)$$

$$E_{\text{diss}}(n) = H_I^f + H_I^m - E_{\text{fc}}(n), \quad (4.7)$$

are forward and reverse reaction rates describing the capture and emission of I from clusters.  $r_n$  is the capture radius for I at clusters of size  $n$ . The quantity  $E_{\text{diss}}(n)$  is the dissociating energy of cluster of size  $n$ . The prefactor  $R_{n_0}$  has a basic physics meaning of attempt frequency for I release. The quantity  $E_{\text{fc}}(n)$  is the formation energy of clusters of size  $n$ .  $H_I^f$  and  $H_I^m$  are the enthalpy of formation and enthalpy of migration of Si interstitial, respectively. Schematic description of the formation energy and dissociation energy, as well as the effect of Si surface is shown in Fig. 5. Si interstitials are

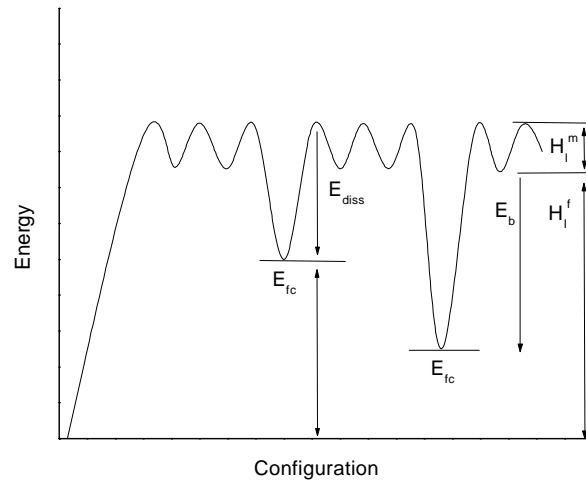


Fig. 5. Schematic description of the formation energy and dissociation energy of extended defects in Si.

emitted from defects with high formation energy, then diffuse and are captured by defects with lower formation energy or by other sinks like Si surface.

The transient interstitial supersaturation  $C_I$  can be determined by measuring the TED of B-doped marker layers using Eq. (4.3). Inverse-model analysis of the supersaturation of interstitials leads to the quantity  $E_{fc}(n)$  for interstitial clusters ranging from a few atoms in size to a few hundreds atoms [77]. Fig. 6 shows the dissociation energy for different clusters obtained from Cowern et al.'s studies [77]. For interstitial clusters with size  $n > 15$ , the energies of formation are around 0.8 eV. For clusters with size  $n < 10$ , the energies of formation are typically 0.5 eV higher. There are two stable cluster sizes at  $n \sim 4$  ( $E_{fc} \approx 1.0$  eV) and  $n \sim 8$  ( $E_{fc} \approx 0.6$  eV).

#### 4.3. Annealing of {3 1 1} defects

It is generally agreed that most of the implantation damage is removed during the early stage of annealing via point defect recombination, leaving excess interstitials approximately equal in number to the implanted dose(+1 model) [87]. These interstitials then coalesce into extended defects. After a short annealing these extended defects are the primarily {3 1 1} defects [82]. Transmission electron microscopy measurements of the total interstitial density in {3 1 1} defects as a function of annealing

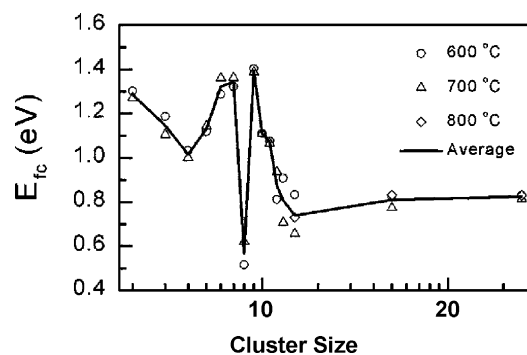


Fig. 6. Dissociation energies of interstitial clusters in silicon (taken from [77]).

time show that the emission of interstitial from  $\{3\ 1\ 1\}$  defects is the main source of interstitials responsible for TED after annealing of small clusters.

The overall equation governing cluster kinetics is given by

$$\frac{dC_{I-cl}}{dt} = 4\pi r D_I C_I C_{I-cl} - C_{I-cl} \nu_0 \exp\left(-\frac{E_{diss}}{k_B T}\right), \quad (4.8)$$

where  $C_{I-cl}$  is the amount of interstitials stored in clusters. The first-term describe the trapping of interstitials by a cluster with capture radius  $r$ . The second term describes the dissociation of interstitials from a cluster, with attempt frequency  $\nu_0$ . The quantity  $\nu_0$  is simply associated to the quantity  $D_I$  by

$$D_I = \nu_0 a^2 \exp\left(-\frac{H_I^m}{k_B T}\right), \quad (4.9)$$

where  $a$  is the average interatomic spacing. When trapping and evaporation reach a balance, equating the first and second terms in Eq. (4.8) yield the interstitial concentration [83]

$$C_I = \frac{1}{4\pi r a^2} \exp\left(-\frac{E_b}{k_B T}\right), \quad (4.10)$$

where  $E_b$  is the binding energy of clusters:

$$E_b = E_{diss} - H_I^m. \quad (4.11)$$

Eq. (4.10) shows that the interstitial supersaturation after balancing between cluster dissociation and growth is independent of the density of clusters. This explains the observation of experimental data that enhancement in diffusivity is constant during transient diffusion [83].

The loss of interstitials from the cluster region is controlled by the diffusive interstitial flux to the surface, which can be approximated by  $D_I C_I / R_p$ , where  $R_p$  is the projected range ion range [83]. Therefore, the time to dissolve  $Q$ , the total interstitials per unit area, is given by [83]:

$$\tau = \frac{Q R_p}{D_I C_I}. \quad (4.12)$$

The activation energy to anneal out  $\{3\ 1\ 1\}$  defect is around  $3.8 \pm 0.2$  eV [83].  $\{3\ 1\ 1\}$  defects can be formed at both amorphizing and sub-amorphizing doses, even when the implantation energy as low as 1 keV [88]. High resolution transmission electron microscopy study observed stable  $\{3\ 1\ 1\}$  defects as shallow as 30 Å from the surface. Although the surface can be a perfect sink for interstitials, excess interstitials near the surface are not annihilated fast enough and hence they still can coalesce into  $\{3\ 1\ 1\}$  defects [88].

#### 4.4. Annealing of dislocation loops

When the implantation dosage is high enough to produce amorphization, dislocation loops may take a long time to anneal out. The structure of the dislocation loops has been analyzed [89,90]. Transmission electron microscopy studies show that annealing of dislocation loops satisfy the Ostwald ripening theory in which the mean radius of the loop increases with time while the total loop density decreases. However, contrary to  $\{3\ 1\ 1\}$  defects, the total number of Si atoms stored in these



dislocation loops remains constant, thus resulting in a local supersaturation of Si interstitials only [91,92]. A fuller thermodynamic account has been given by the same authors which predicted that the mean size of the dislocation loops would vary as  $1/t$  and the mean radius increased as  $t^{1/2}$ , in agreement with experimental results. Studies on defect evolution indicate that the activation energy for loop growth is around 1–2 eV for shorter annealing times or lower temperatures. For longer annealing time under higher temperatures (e.g. 900 °C, >30 s), the activation energy for growth is around 4.5 eV, a value close to that for self-diffusion in Si [90].

#### 4.5. Boron clustering in extrinsic TED

In most cases, electrical measurements of implanted B after annealing showed boron was not fully activated. This is especially true for high dose implantation. A static, electrically inactive B peak was usually observed above a critical concentration which is below solid solubility of B in Si, but correlates closely with intrinsic carrier concentration  $n_i$ . A comparison of the critical concentration,  $n_i$ , and B solubility [73] has shown that the critical concentration has no strong dependence on implantation energy [78] and is independent of dose over a wide temperature range of 650–900 °C [73,93]. It was suggested that the high concentration of free interstitials immediately following implantation interacts with substitutional boron atoms to form boron interstitial precursors. These dopant clusters bind strongly and may further capture mobile boron interstitials. The boron clusters would gradually release their interstitials during annealing and leave behind stable boron interstitial clusters [94]. B clustering can be described as



where  $B_s$  refers to substitutional B atoms,  $B_i$  to mobile B atoms and  $B_C$  to immobile clusters containing  $(m + 1)$  B atoms, while  $n$  is the number of Si self-interstitials ejected upon clustering. The B clusters are metastable and would dissolve upon further high-temperature annealing [83].

#### 4.6. The role of the surface in TED

Lim et al. [95] measured the reduction in the TED of a buried B marker as a function of distance from the surface following a medium energy (40 keV) Si implantation. They found that more than 99% of all interstitials recombine at surface during a 2 h, 800 °C annealing. On the other hand, Omri et al. [96] reported a negligible contribution of surface to the formation of end of range (EOR) defects provided that the surface was preamorphized. The discrepancy may be due to different methods (diffusivity versus loop density) to identify interstitial supersaturation and hence surface recombination. Furthermore, both studies employed surface etching which may have modified the surface.

Agarwal et al. [97] varied the distance of the implanted region to the surface by varying the ion implantation energy and measured the enhanced diffusion of buried boron markers to monitor the excess interstitials that diffuse into the bulk at 810–1050 °C. Interstitial annihilation at surface has been quantified as a function of distance of the excess interstitials from surface while maintaining the same surface condition for all samples (using chemical etching). They demonstrated that TED from a silicon implant decreased linearly with Si ion implantation energy, and predicted that TED driven by Si interstitials would *disappear* with implantation of Si at energies lower than 1 keV. However, for sub keV-B implantation, anomalous B diffusion still persisted [98]. This phenomenon will be discussed in the following section in more detail.

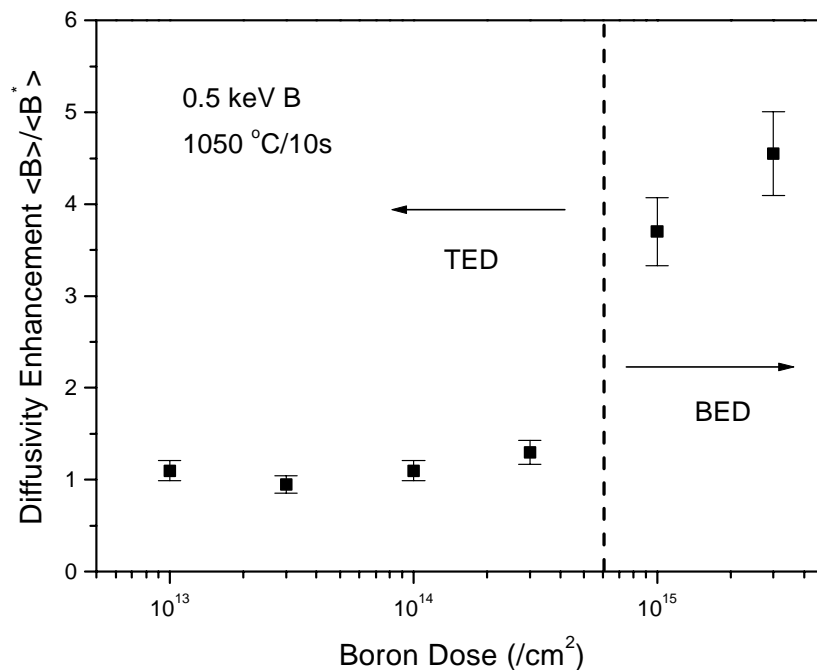


Fig. 7. Diffusivity enhancement of boron from 0.5 keV B implanted at different dosage (from [98]).

#### 4.7. Boron enhanced diffusion (BED)

TED of grown-in B markers caused by implantation of  $1 \times 10^{14} \text{ cm}^{-2}$  Si atoms decreases linearly with the incident energy of Si ions. TED from sub-keV Si implantation is virtually eliminated. This implies possible disappearance of transient-enhanced diffusion of B for sub-keV B implants. However, when implanted species was changed from silicon to boron, enhanced diffusion of boron was still observed [98,99]. It has been proposed that the formation of the silicon boride phase (probably silicon triboride  $\text{SiB}_3$ , or silicon tetraboride  $\text{SiB}_4$ ) creates an interstitial supersaturation, in a way similar to silicon dioxide [98,99]. This boron-enhanced diffusion is only observed when the concentration of boron exceeds a certain threshold [98,99]. For 0.5 keV B implantation, this threshold concentration corresponds to an implantation dosage of  $1 \times 10^{15} \text{ cm}^{-2}$  (see Fig. 7). This happens to be the threshold B dose to amorphize Si. Previous study has shown that formation of silicon boride phase in crystalline Si needs an extremely high thermal budget [100], i.e. several tens of hours at 1000 °C. It is suggested that the kinetic barrier to silicon boride phase formation might be considerably reduced in amorphous silicon as opposed to crystalline silicon [98]. Different from TED, where the B anomalous diffusion is driven mainly by the dissolution of the defects containing only self-interstitials. The BED is assumed to be driven by released Si interstitials from Si–B complexes. Furthermore, TED is usually associated with ion bombardment induced damages while BED can be observed in ultra-low energy B-implanted layer, as well as evaporated boron layer without implant damages [98].

In addition to BED, another boron induced diffusion enhancement is called couple diffusion of B (or chemical pumping effect). In this mechanism, enhanced diffusion of B arises from the high B concentration gradient from the silicon surface into the bulk of the crystal [101]. Since boron diffusion proceeds by interacting with Si interstitials, boron behaves like a carrier, absorbing a Si

interstitial and releasing it deep into the bulk via reaction  $B_i \rightarrow B_s + I$ . The buildup can be sustained because the surface is an essentially free source/sink for  $I$ , and so the transport of  $B_i$  into the crystal is compensated for by the generation of additional interstitials at the surface [74,101]. According to modeling, the couple diffusion of  $B$  is the major contribution to diffusion enhancement at low temperature, while BED dominates the enhanced diffusion when annealing temperature is above around 950 °C [98].

Recently, the kinetics of self-interstitials release in a BED reaction was studied using MBE B-doped Si superlattices [99,102], in which a highly doped Si layer was used as a source of boron to induce BED. B delta-doped layers, grown by molecular beam epitaxy (MBE) on a p-type, 15–25  $\Omega$  cm Si wafer, were used as diffusion markers. The four B-doped layers above the Si substrate, each with approximately  $3 \times 10^{19} \text{ cm}^{-3}$  peak concentration, are separated by 100 nm of Si. The fifth layer was 10 nm thick with a B concentration of  $10^{21} \text{ cm}^{-3}$  ( $\sim 2$  at.%). A 100 nm undoped silicon cap layer above the top boron-doped layer is used to avoid surface complexities such as B flux effect and loss of B during annealing [99]. MBE superlattice growth uses electron-beam evaporator as Si source, with a typical Si growth rate around 0.1 nm/s. B was introduced by evaporation of elemental B. The substrate was stabilized at 500 °C when boron was delta doped. This temperature helps facilitate an excellent profile control without precipitation and surface segregation effects. Fig. 8 shows the SIMS measurements of B depth profiles in the as-deposited sample and the samples annealed at 800 and 900 °C for various times. Significant B diffusion is observed upon annealing at the temperature above 900 °C, with the topmost B layer displaying the most substantial broadening. It is obvious from the spike closest to the topmost B layer that the spike experienced more diffusion than the

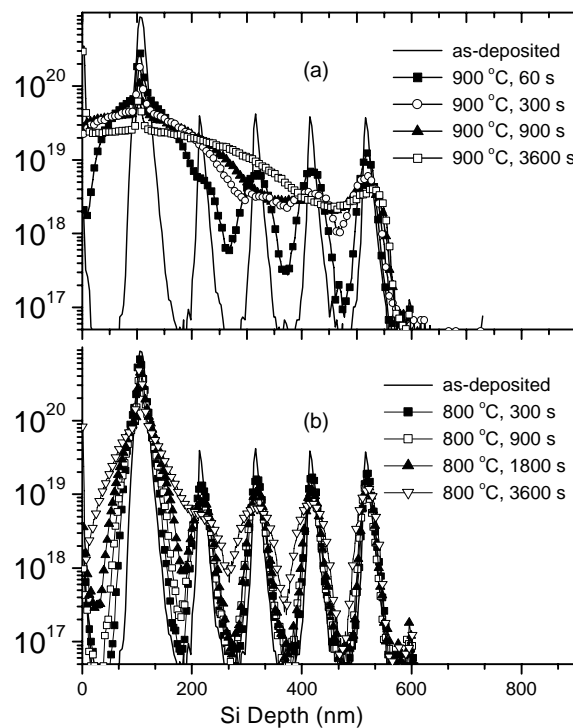


Fig. 8. SIMS profiles of B in B-doped Si superlattices grown by MBE, annealed at 800 and 900 °C for various time. BED is observed, and BED is reduced when the markers is away from the source which is located near 100 nm [102].

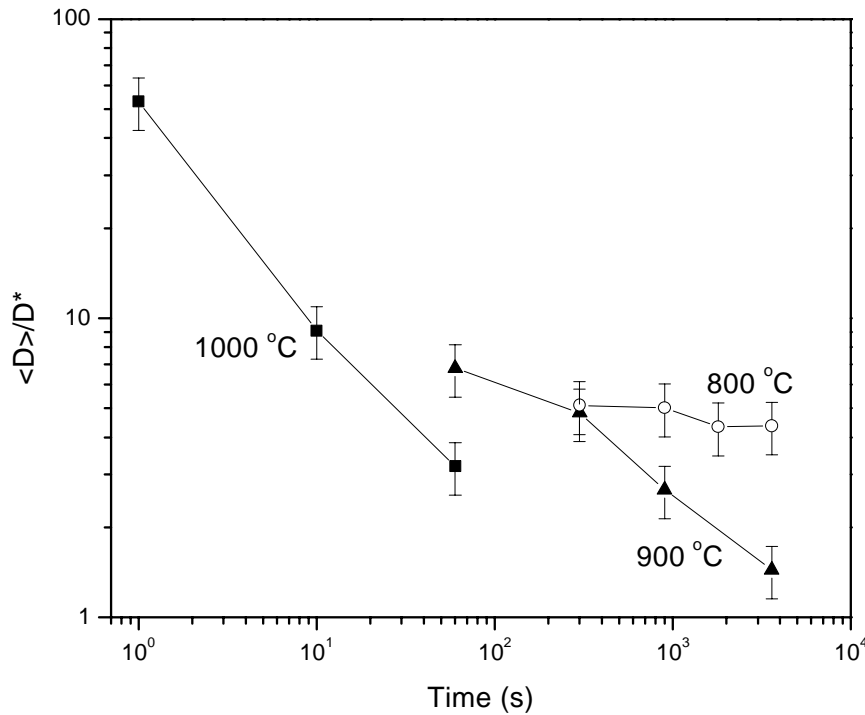


Fig. 9. Plot of the time-averaged boron diffusivity enhancement of spike 4 vs. time [102].

deeper layers. This implies that the Si self-interstitials were injected from the high concentration B layer to the deeper layers. Fig. 9 shows the normalized time-averaged diffusivity of spike extracted from SIMS profiles. It shows that B diffusion is mediated by a supersaturation of interstitials. The different slopes indicate that the decay in the source of interstitials is temperature dependent with a transient burst of interstitials taking place at 1000 °C and a slow decay at 800 °C. The decay time of the interstitials emission from BED source was further studied. Fig. 10 shows an Arrhenius plot of the decay time as a function of annealing temperature. The kinetics of diffusion of B from the marker shows that the enhanced B diffusion is governed by the release of Si interstitials with an activation energy of  $3.9 \pm 0.2$  eV [102].

Having established the activation energy  $E_m + E_b = 3.9$  eV and taking the interstitial migration energy  $E_m = 1.77$  eV from Zn diffusion experiment [7], the binding energy of Si interstitials in BED defects is given by  $E_b = 2.1$  eV. This high value indicates that BED should be expected only at a relatively high temperature. This is consistent with the negligible diffusion observed at 720 °C. The value 3.9 eV is close to the 3.8 eV for the Si interstitials released from {3 1 1} defects as reported by Stolk et al. [83], but far from the 1.7 eV for Si interstitials released from silicon boron clusters produced in the sub-keV B implant [103,104]. It is believed that these two very different activation energies originate from quite different defect structures [102], with the lower energy case more plausibly being attributed to the weakly bound excess interstitials [103].

For all practical purposes, ultra-shallow boron junctions require high concentration of boron with minimum diffusion in Si. Unless a different approach is obtained, occurrence of BED puts an insurmountable processing limit on the ultra-shallow junction. PDE is perhaps one of the most promising solutions, as will be elaborated in the next section.

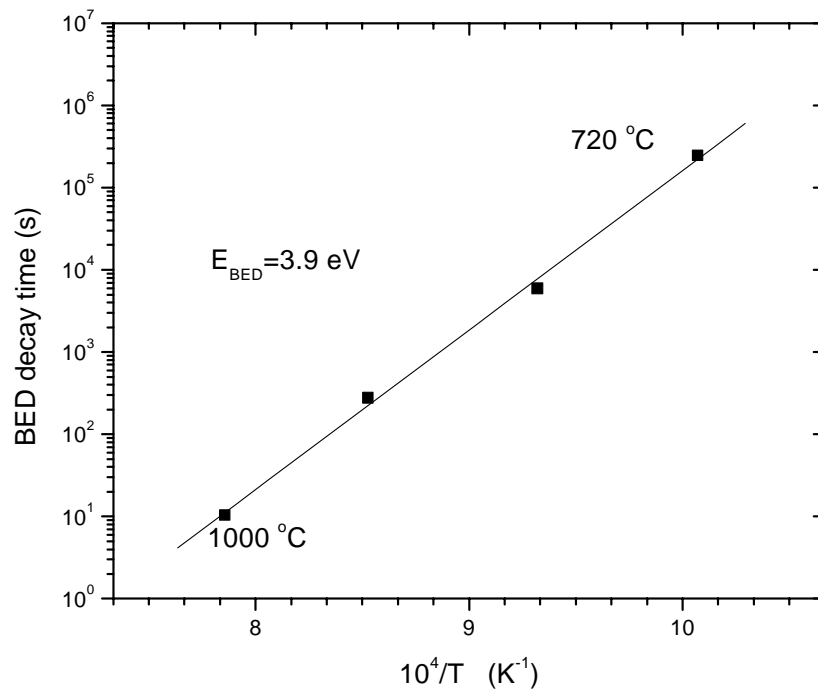


Fig. 10. Arrhenius plot of the BED component decay times [102].

## 5. Point defect engineering and its application in boron diffusion control and ultra-shallow junction formation

### 5.1. Defect imbalance induced by high-energy ion implantation

In the so called “+1 model” proposed by Giles [87], nearby vacancies and interstitials recombine either dynamically during irradiation or subsequently during post-implant annealing. Extra atoms corresponding to the implant dose at end of range defect position are responsible for TED. However, the momentum transfer from an incident ion is in the forward direction, hence the depth profile of interstitials would naturally be slightly deeper than that of vacancies. Due to the dynamic annealing of Frenkel pairs in close proximity, a vacancy rich region is formed close to the surface while excess interstitials are left in the end of range region of the incident ions [105]. Fig. 11 shows the results of a TRIM [106] simulation of the excess defect population created by 50 keV or 500 keV Si implants. It reveals the formation of a net vacancy-rich region with a depth around half of the Si projected range. The average separation between vacancy locations and interstitial locations increases with the implantation energy. The dashed lines in Fig. 11 are the plots of the distribution of extra atoms inside the Si substrate, introduced by implantation and the solid lines are the defect distribution of interstitials and vacancies from spatially separated Frenkel pairs, where negative concentration indicates vacancies and positive concentration indicates extra Si self-interstitials or excessive Si implants. It is obvious that the depth distribution of vacancies and self-interstitials in Si can be tailored by selecting the energy of Si implantation. Fig. 12 demonstrates the average separation between extra vacancies and extra interstitials can be enlarged by increasing the energy of incident ions. This average separation can be approximately described by  $R_p - \Delta R_p$ ,

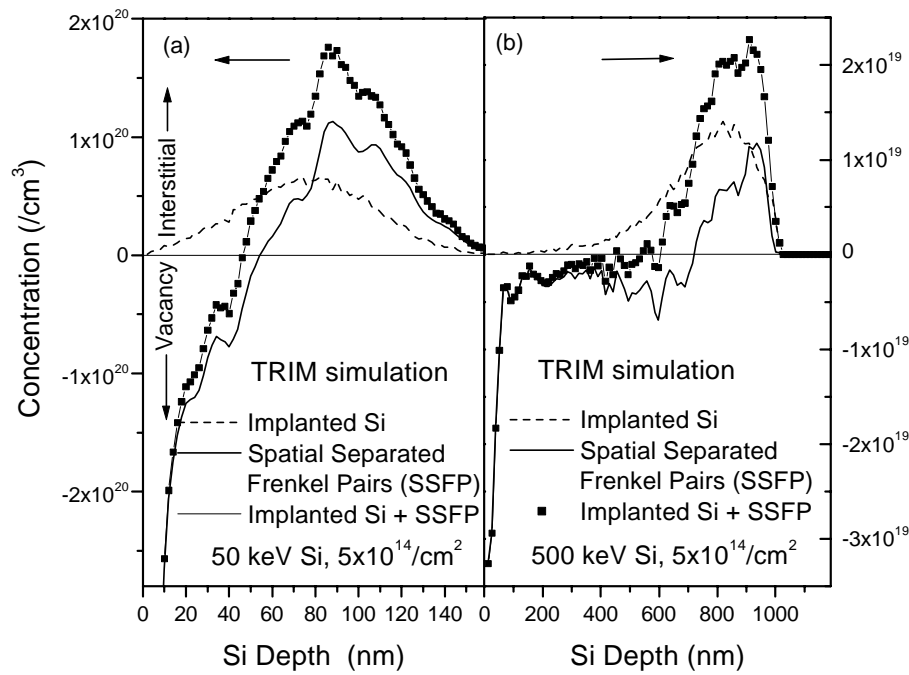


Fig. 11. TRIM simulation of (a) 50 keV and (b) 500 keV Si ions implanted into Si to a dosage of  $5 \times 10^{14} \text{ cm}^{-2}$ . The dashed lines are plots of the distributions of extra atoms introduced by implantation and the solid lines are plots of the defect distribution of interstitials and vacancies from spatially separated Frenkel pairs. A negative concentration indicates extra vacancies while a positive one indicates extra interstitial defects [112].

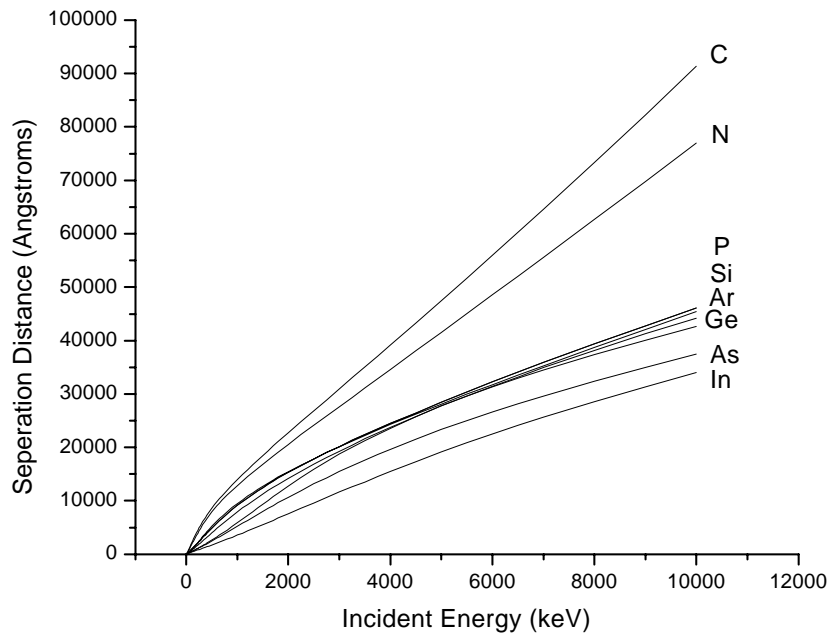


Fig. 12. Separation of vacancy and interstitial rich region as a function of the incident energy of different ions.

where  $R_P$  is the projected range and  $\Delta R_P$  is the range straggling of the incident ion. I–V separation distance is related to the stopping power of incident ions in Si. Usually, the lighter ions penetrate more deeply and result in larger separation. Light ions, however, need high-dosage implantation to create enough defects. We prefer Si or Ge ions for PDE application because all chemical complication due to other ions can be avoided.

### 5.2. Reduction of boron TED in silicon

Many authors have observed the reduction of boron TED with high-energy implantation (HEI). Reduction of the transient diffusion of B in silicon by co-implantation with MeV Si ions has been reported by Raineri et al. [107], although they explained it as being due to the secondary defects, formed by MeV implantation, acting as efficient sinks for Si interstitial. Using the method of co-implantation with high-energy Si into SOI wafers, Holland et al. [108,109] showed the reduction of boron enhanced diffusion without the effect from MeV implantation-induced end of range defects. More recently, using a B superlattice structure grown on SOI wafer, Venezia et al. [110] clearly demonstrated that such reduction was due to the vacancy-rich surface region created by the MeV Si implantation. In their studies, a buried  $\text{SiO}_2$  layer (around 750 nm deep) is used to isolate the excess interstitials from the excess vacancies created by the MeV Si implant. Molecular beam epitaxy grown B dopant markers were used as an interstitial detector. Observed B TED suppression, as shown in Fig. 13, supports that reduced interstitial supersaturation is due not to the

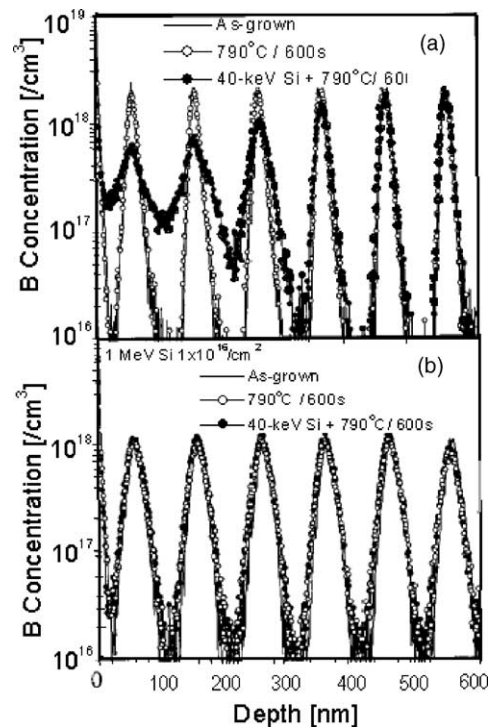


Fig. 13. (a) B profiles of B-delta-doped samples implanted with 40 keV Si to a dose of  $5 \times 10^{13} \text{ cm}^{-2}$  and annealed at 790 °C for 600 s. Also included in the figure are profiles from an as-grown and control B samples. (b) B concentration profiles of samples implanted with 1 MeV Si ions to a dose of  $10^{16} \text{ cm}^{-2}$  followed by a 790 °C, 600 s anneal, or a 40 keV Si  $5 \times 10^{13} \text{ cm}^{-2}$  implant and 790 °C, 600 s anneal [110].



gettering by end of range defects but to the excessive vacancies created by MeV implantation. Furthermore, a significant reduction in secondary defect formation (such as dislocation loops, line defects) in the B implantation region has been observed with high-energy silicon co-implantation [110].

### 5.3. Reduction of BED in silicon

As mentioned above implantation of MeV Si ions into a Si substrate can also suppress boron-enhanced diffusion normally associated with a high B concentration layer [111–115]. A molecular beam epitaxy grown Si layer with a B concentration of  $10^{21} \text{ cm}^{-3}$  over a 10 nm region capped with 100 nm Si was used as a source of BED. A sequence of four B delta-doped layers with 100 nm Si spacers was grown prior to the source layer to monitor the diffusion. Half of the sample was implanted with 1 MeV Si ions at a dose of  $10^{16} \text{ cm}^{-2}$ , followed by annealing at 800, 900 and 1000 °C for different periods of time. Fig. 14 shows the SIMS measurement of B depth profiles in the as-deposited MBE sample, and samples implanted with MeV Si ions to a dose of  $10^{16} \text{ cm}^{-2}$ , annealed at 800 °C or 900 °C for 1 h. Significant B diffusion in the unimplanted samples was

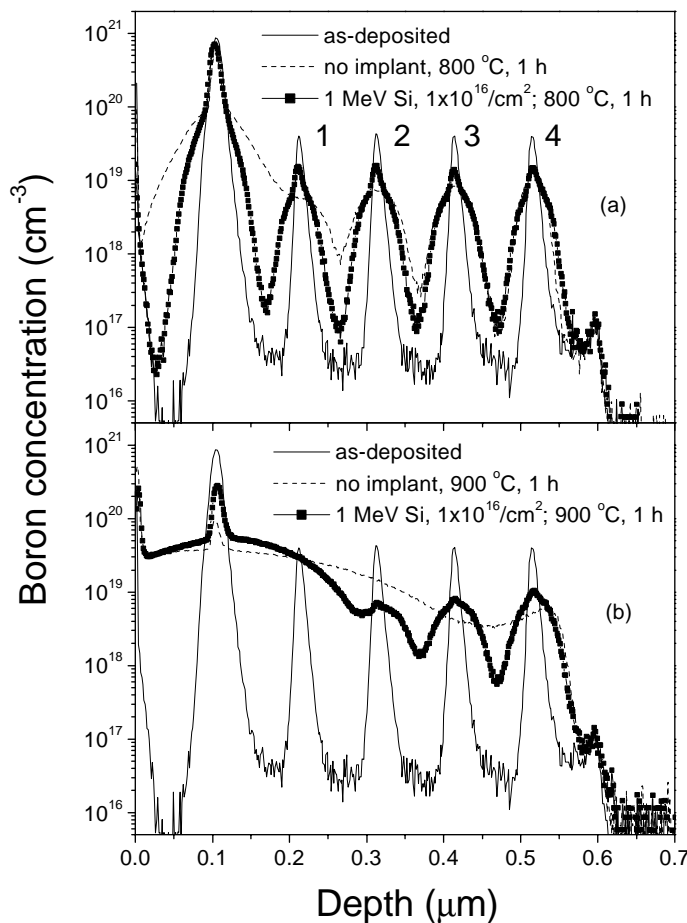


Fig. 14. SIMS profiles of boron with or without MeV Si ion implantation [114].

observed upon annealing, with the topmost B layer showing most substantial broadening. However, the samples that are implanted with MeV Si ions show much less diffusion. After the 800 °C, 1 h anneal, the Si MeV implant was most effective in inhibiting the B diffusion in B spikes 1 and 2 and had no effect in spikes 3 and 4. After the 900 °C, 1 h anneal, the Si MeV implant had no measurable effect on the diffusion of B in spike 1 (it may have been masked by the B diffusion from the topmost layer.) and was increasingly more effective in spikes 2–4.

Assuming an initial  $\delta$ -function B distribution, the one-dimensional spatial distribution of the dopant concentration profile has been established to be Gaussian-like upon high-temperature annealing but is exponential-like for low temperature annealing [75]. Under the circumstance that mean number of migration events ( $n$ ) is much larger than one, or  $n \gg 1$ , Gaussian profile fitting as governed by Fick's law is valid. Spreading of a Gaussian distribution satisfies  $w^2 = w_0^2 + 2 \int D_B dt$ , where  $w$  and  $w_0$  are the half width of the Gaussian fitting before and after annealing. The enhanced diffusivity thus reflects the local concentration of self-interstitials as  $\langle D_B \rangle / D_B^* \sim \langle C_I \rangle / C_I^*$ , where  $C_I^*$  is the equilibrium concentration of self-interstitials,  $\langle C_I \rangle$  is the time-averaged local concentration of self-interstitials and  $\langle D_B \rangle$  is the time-averaged B diffusivity.

Fig. 15 shows the normalized time-averaged diffusivity  $\langle D_B \rangle$  extracted from the SIMS profiles in Fig. 14. The diffusivity of the topmost B layer was also calculated by ignoring high concentration effects. Extraction of diffusivities for control sample after 900 °C 1 h anneal is not possible since diffusion from spikes 1–4 was masked by the significant diffusion from the topmost layer. The experiment diffusivity was divided by the equilibrium B diffusivity  $D_B^*$ ,  $4.26 \times 10^{-17} \text{ cm}^2/\text{s}$  at 800 °C. A significant suppression of BED for the implanted samples annealed at 800 °C for 1 h has been observed. It shows an average diffusion enhancement factor of  $\sim 8$ .

Fig. 16 shows the SIMS profiles of samples annealed at 1000 °C for periods of 1 and 60 s. Significant diffusion after annealing at 1000 °C for 1 s indicates a large enhancement of diffusion in the early phase of annealing. Fig. 17 shows the evolution of diffusivity enhancement extracted by fitting the profiles in Fig. 16 according to broadening  $l = \sqrt{w^2 - w_0^2} = \sqrt{2 \int D dt}$ . Thickness of the capping layer above the first boron layer is 100 nm, which was so intended that it's close to the reported surface recombination length ( $L \sim 100 \text{ nm}$ ) [95]. Therefore, a larger diffusion enhancement is expected in comparison with the result from surface boride layers, e.g. an

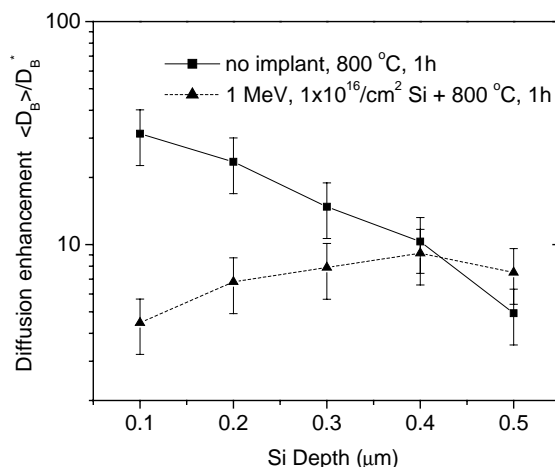


Fig. 15. Boron diffusivity enhancement vs. depth, extracted from the diffusion profiles in Fig. 14. Samples were implanted with 1 MeV  $10^{16} \text{ cm}^{-2} \text{ Si}^+$  ions and annealed at 800 °C for 1 h [114].

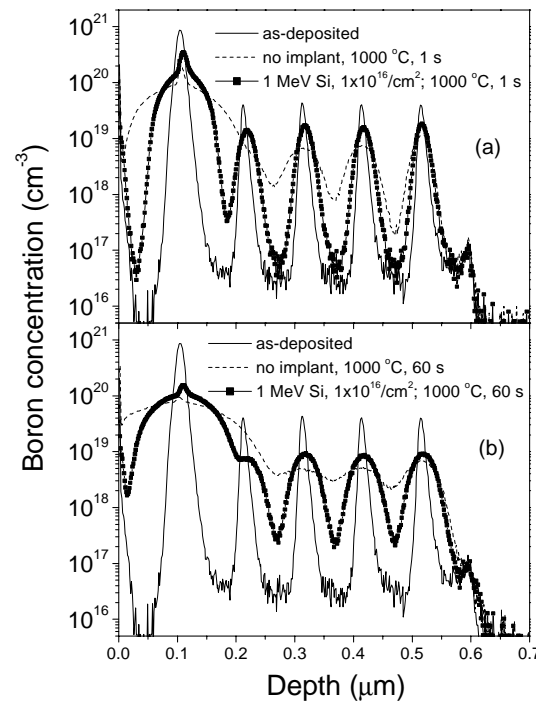


Fig. 16. SIMS showing B diffusion after annealing at 1000 °C for periods of 1 s (a), and 60 s (b). Samples with 1 MeV  $10^{16} \text{ cm}^{-2} \text{ Si}^+$  implant (the squares) show suppressed diffusions in comparison with non-implanted one (the dashed lines) [114].

enhancement fact of  $\approx 4$  [98,99]. The time-averaged enhancement,  $\langle D_B \rangle / D_B^*$ , is around 40, 13, and 5, during the periods from 0–1, 1–10, and 10–60 s, respectively. Similar transient behaviors of BED have been observed in a previous study [116]. For the samples with MeV implant, the BED is smaller, yet nonvanishing.

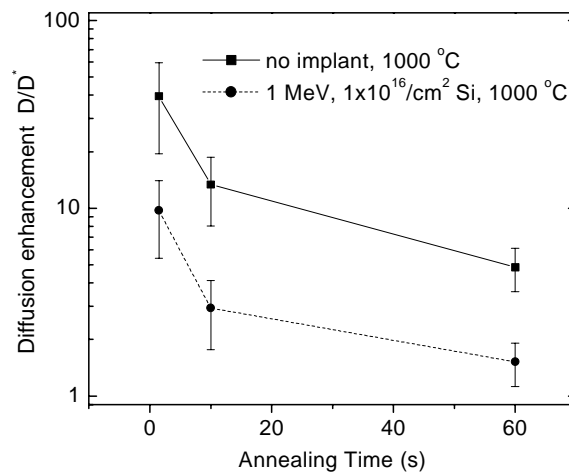


Fig. 17. Averaged diffusion enhancement for spikes 2–4 as a function of annealing time at 1000 °C. The squares refer to annealed sample with 1 MeV Si implantation to a dose  $10^{16} \text{ cm}^{-2}$ , and the circles to the non-implanted samples [114].

Recent studies on vacancy effects in Sb diffusion indicated that the decay of vacancy supersaturation occurred on a short time scale [117]. It has been confirmed by Venezia et al. [118] that a high degree of supersaturation of single vacancies occurs within a short time during annealing at 700–900 °C, followed by a relaxation back to equilibrium with the formation of stable vacancy clusters. If the vacancy supersaturation in the near surface region decays on a faster time scale than the release of interstitials from the BED source, considerable BED will still exist. The reduction of the normalized diffusion with time in the implanted samples, as shown in Fig. 17, indicates that the suppression of BED is not complete, interstitial defects coming from the end of range defect by MeV implant may also come into play at a relatively high temperature annealing.

#### 5.4. Ultra-shallow junction formation

The effect of high-energy ion implant on the diffusion of boron from surface deposited B layer has been studied [111,112]. The 20  $\Omega$  cm n-type Czochralski-grown Si (1 0 0) wafers were implanted with 500 keV  $5 \times 10^{14}$  cm $^{-2}$  Si at room temperature. Then 10 nm thick boron layers were deposited onto ion implantation irradiated substrate by electron-gun deposition. HF etch was performed both before implantation and before deposition to remove the native oxide. Deposition was performed at a rate of 0.1 nm/s under a base pressure of argon at  $3 \times 10^{-6}$  Torr. After deposition, samples were annealed at 900 °C or 950 °C or 1010 °C for 15 s, using a rapid thermal processor AG Associate Heatpulse 210 T under continuous N $_2$  flow. Fig. 18 shows the SIMS profiles of diffused boron from a surface deposited layer into ion implantation damaged Si substrate. It is obvious that there is a reduced diffusion in 500 keV-irradiated samples when compared with the non-irradiated sample in all three annealing conditions.

Fig. 19 shows the spreading resistance profiles of the samples, which were first implanted with 500 keV Si $^{+}$  ions to a dose of  $1 \times 10^{14}$  cm $^{-2}$  or  $5 \times 10^{14}$  cm $^{-2}$ , respectively, then 10 nm of boron was deposited on the Si substrate. Subsequent annealing was at 900 °C for 10 s. It is shown that when the Si dose implanted is increased, the profile of B carrier concentration becomes shallower. The spreading resistance profile of the sample implanted with 500 keV to a dose of  $5 \times 10^{14}$  cm $^{-2}$

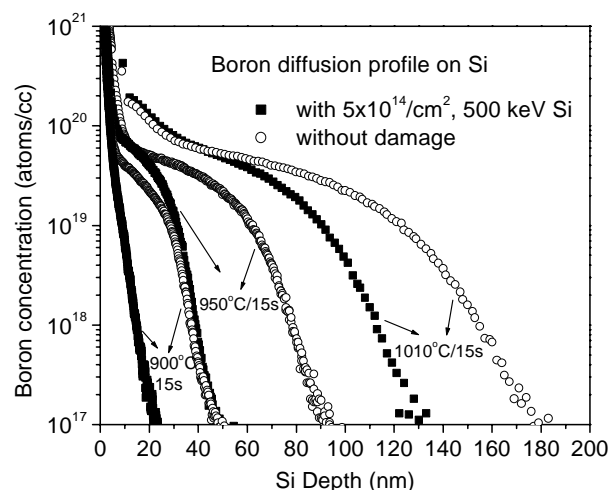


Fig. 18. SIMS profiles of diffused boron from surface deposited layer into ion implantation damaged substrate. Sample were first implanted by  $5 \times 10^{14}$  cm $^{-2}$  Si ions with 500 keV incident energy. Then 10 nm thick boron layer are deposited onto Si substrate by e-gun evaporation. The samples were subsequently annealed at 900 °C, 950 °C, or 1010 °C for 15 s [114].

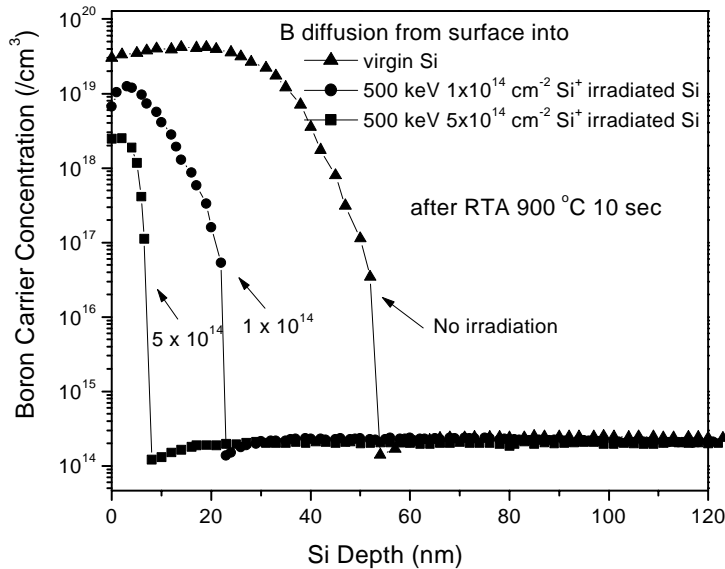


Fig. 19. Spreading resistance profiles of samples first implanted with 500 keV Si ions to a dose of  $1 \times 10^{14}$  or  $5 \times 10^{14} \text{ cm}^{-2}$ , respectively, followed by deposition of a 10 nm layer of boron. Subsequent annealing was at  $900^\circ\text{C}$  for 10 s (Shao et al.). Surface carrier concentration of the shallowest junction was underestimated due to the limitation of spreading resistance measurements [112].

shows a junction depth as shallow as 6 nm measured at  $1 \times 10^{17} \text{ cm}^{-3}$ , while the sheet resistance comes out to be  $1200 \Omega/\square$ . However, the surface carrier concentrations shown in Fig. 19 were actually underestimated since such shallow junctions are approaching the limits of spreading resistance measurements. Since older gas-phase doping concept is now being revived for scaled devices with improved concentration control [119–121], it shows great potential in shallow junction formation by combining defect engineering with thermal diffusion. Complete removal of end of range damage is desirable since the presence of dislocation loops in the depletion region of a junction degrades device performance. However, end of range loops are harmless when they are deep into the substrate and remote from the depletion region. In the MeV co-implantation experiments reported by Saito et al. [122,123], the junction depth of 10 keV B implants was reduced by adding 1 MeV  $\text{F}^+$  implants. Carrier activation is the same with or without MeV implants, but the MeV  $\text{F}^+$  implanted samples have lower junction leakage currents than that of the control samples.

The complication of interstitial defects can be further eliminated by using silicon-on-insulator wafer in which a buried  $\text{SiO}_2$  served as a diffusion barrier for the interstitials. Fig. 20 shows the SIMS profiles of B after annealing at  $980^\circ\text{C}$  for 1 s. B was deposited on the Si substrate with a thickness around 0.4 nm. Prior to B deposition, the Si was bombarded with 1 MeV Si ions with dosage ranging from  $1 \times 10^{14}$  to  $3 \times 10^{15} \text{ cm}^{-2}$ . B penetration was suppressed for implanted Si. Sub-10 nm junctions can be formed by the strategy.

In the case of using B implantation for shallow junction formation, most of previous works have concentrated only on the diffusion of TED with B energy at a few keV to 40 keV, instead of the desired sub-keV B implants where BED dominates junction spreading. To study the effect of PDE on sub-keV B implantation, bare (1 0 0)-oriented n-type Si wafers, preamorphized with 5 keV Ge ions, were implanted with 0.5 keV B at a dosage of  $1 \times 10^{15} \text{ cm}^{-2}$ . Ge implantation produced a shallow amorphous region around 12 nm deep. A subset of the wafers additionally received a “PDE” MeV Si ion implantation with a dosage of  $5 \times 10^{15} \text{ cm}^{-2}$ . Annealing is performed under  $\text{N}_2$  ambient at

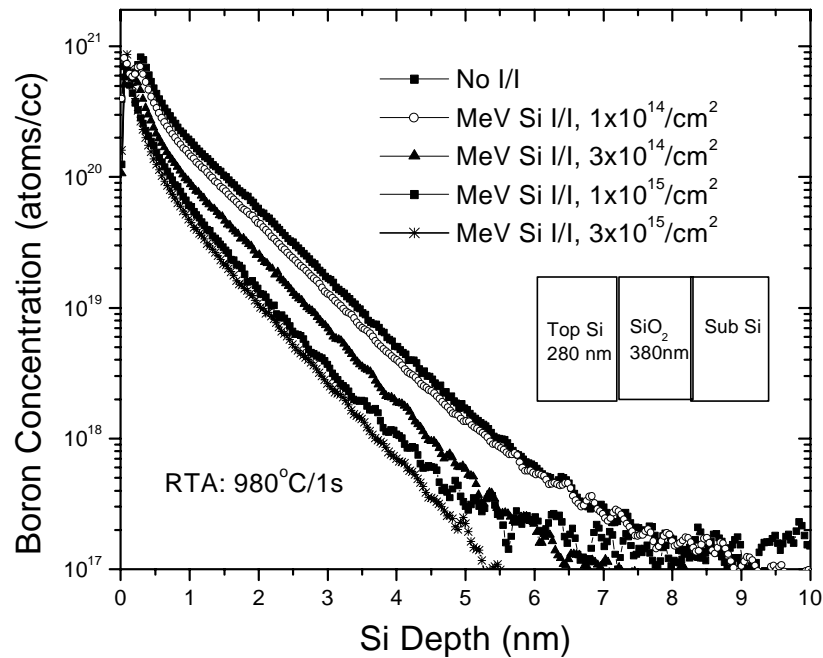


Fig. 20. SIMS profiles of B in the annealed samples first implanted with 1 MeV Si ions with a dosage ranging from  $1 \times 10^{14}$  to  $3 \times 10^{15} \text{ cm}^{-2}$ , then followed by deposition of a 0.4 nm layer of boron. Subsequent annealing was at 980 °C for 1 s. Samples has a buried  $\text{SiO}_2$  380 nm thick with a top Si layer of 280 nm. MeV Si implantation has a range around 1500 nm (deep inside the substrate).

1000 °C for 1 s, or 900 °C for 10 s. Fig. 21 shows SIMS profiles of 0.5 keV B implants after 900 and 1000 °C annealing. It shows that: (1) PDE significantly reduces B diffusivity. After 1000 °C rapid thermal annealing (RTA), junction depth  $X_j$  (measured at  $1 \times 10^{18} \text{ cm}^{-3}$ ) is reduced from 30.8 nm (without PDE) to 21.4 nm (with PDE); (2) PDE makes B profile sharper, by changing profile slope from 13.2 nm per decade to 4.7 nm per decade after 1000 °C RTA; (3) PDE reduces the B clustering. Diffusion of B in PDE sample starts from a concentration much higher than that of control samples.

The reduction of dimensions of CMOS transistor downscaled below the 90 nm node faces two main challenges: reducing junction depth and decreasing the parasitic series resistance. The latter is not only for power saving, but also for improvement of device performance. For this purpose, the international technology roadmap for semiconductors (ITRS) has laid out specifications on the source/drain junction resistance and depth. In particular, the metrics for evaluating the junction efficiency relies on the sheet resistance versus junction depth graph, which determines the regions of “acceptable” junctions properties according to the technology node (see Fig. 22). These requirements become more and more aggressive as the device is further downscaled, in particular for p-type transistors where both boron diffusion and activation are serious issues.

Experimental data obtained using point defect engineering are summarized in Fig. 22, compared with those from other approaches [124]. There is a lower bound for most ion implantation and rapid thermal annealing experiments, as depicted. However, junctions formed by point defect strategy are able to bypass this thermal-dynamical limitation, giving much lower surface resistance not attainable by other traditional methods. PDE is a non-equilibrium thermodynamic process. Artificially generated vacancies modify the boron diffusivity, boron distribution and its solid solubility. This will be covered in the next section.

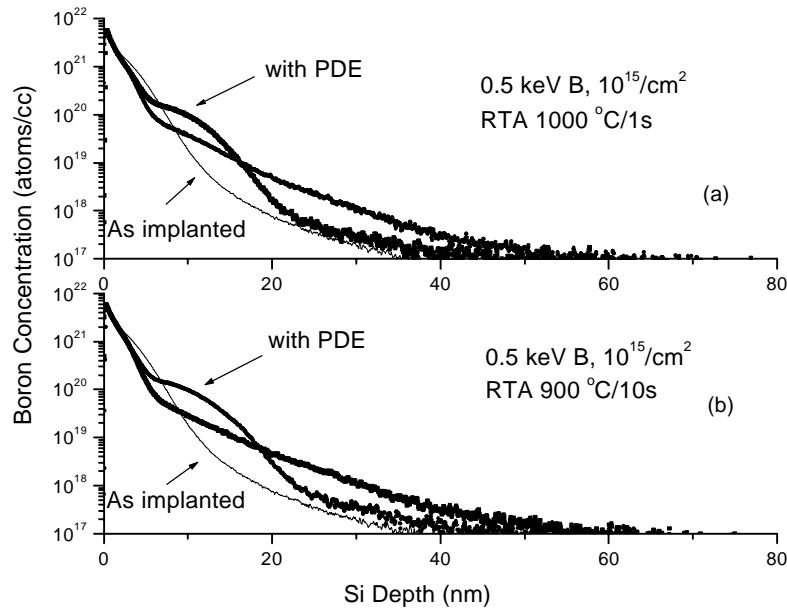


Fig. 21. SIMS profiles of  $1 \times 10^{15} \text{ cm}^{-2}$ , 0.5 keV B implants, with or without MeV Si co-implantation, after annealing at  $1000^\circ\text{C}$  for 1 s (a), or  $900^\circ\text{C}$  for 10 s (b).

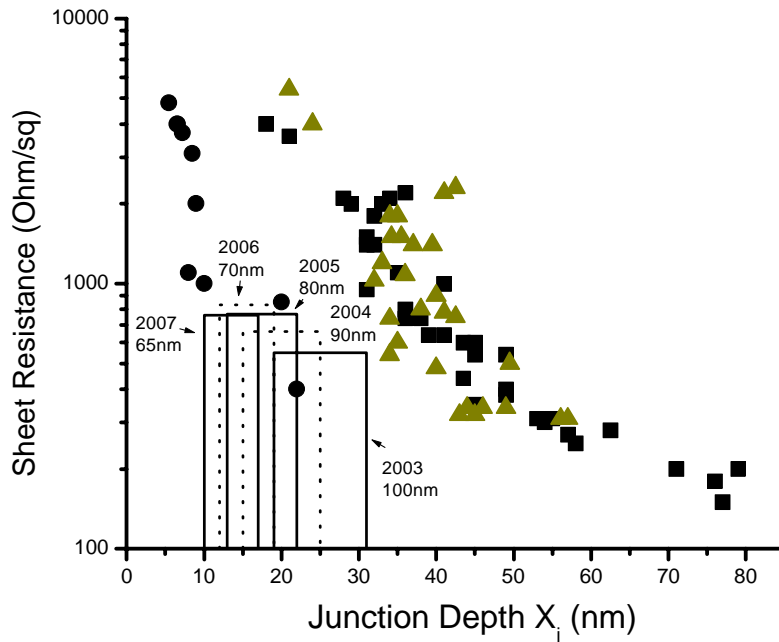


Fig. 22. Experimental data of sheet resistance vs. junction depth. The triangles (refers to B implantation) and squares (refers to B implantation + preamorphization) represent the junctions obtained by traditional methods. The cascade boxes represent the range of international roadmap requirements of transistors for given feature sizes. Circle symbols represent junctions achieved by the point defect engineering method at the University of Houston.



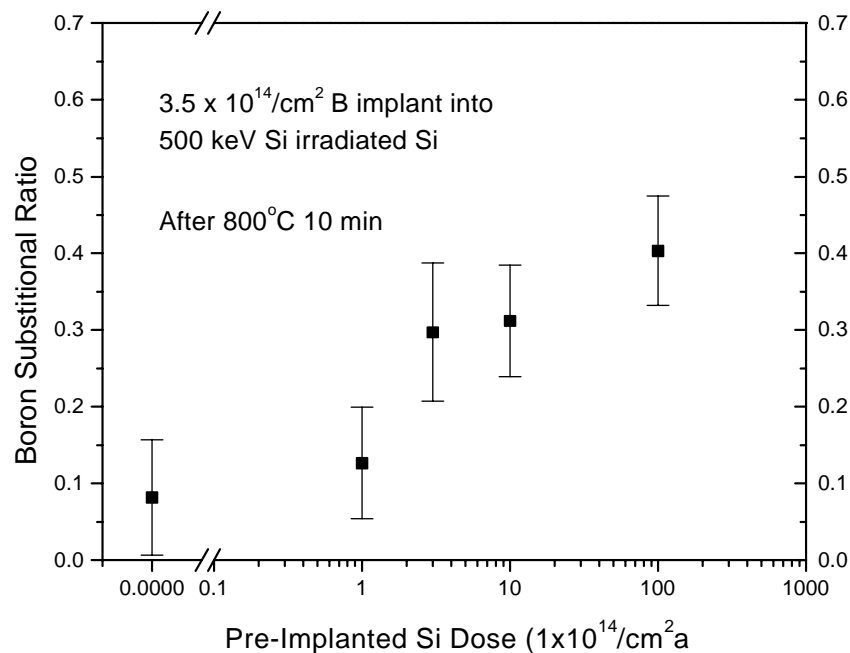


Fig. 23. Nuclear reaction analysis using  $^{11}\text{B}(\text{p}, \alpha)^8\text{Be}$  along the channeling and random direction provides B substitutional fraction for 2 keV implanted B with or without co-implantation of 500 keV Si ions, followed by annealing at 800 °C for 10 min annealing [125].

### 5.5. Enhanced activation of B

It is expected that in the vacancy rich region, reduced Si interstitials will decrease the concentration of boron clusters  $\text{B}_\text{C}$ , and thus enhanced B activation. Reduction of B clustering with high-energy co-implant has been experimentally reported [125]. Fig. 23 shows the substitutional ratio of annealed 2 keV B implants with or without 0.5 MeV Si co-implantation. The substitutional ratio of B was increased to 40% with an enhancement of around 4, when compared with control sample without Si co-implantation [125]. Substitutional ratio of B was measured by nuclear reaction analysis (NRA), using a wide resonance reaction of  $^{11}\text{B}(\text{p}, \alpha)^8\text{Be}(\text{Be} \rightarrow \alpha + \alpha)$ , at a proton energy of around 650 keV. The measurements of  $\alpha$ -particles with protons incidence along a channeling direction and that along a random direction would provide calculation to the amount of substitutional B. Therefore, the fraction of the substitutional boron S can be calculated. Electrical measurement also confirmed enhancement of B activation [125,126]. Fig. 24 shows sheet resistance measurement results of Si and B co-implanted samples after rapid thermal annealing at 400 °C or 600 °C for 10 s, under continuous  $\text{N}_2$  flow. For such a low thermal budget, no profile shifts are observed. Thus, the reduction in the sheet resistance reflects the increase of activated B.

### 5.6. Parameters of PDE for B diffusion control

The efficiency of PDE with respect to the energy of incident ions has been studied recently [112]. The sample was first implanted with  $5 \times 10^{14} \text{ cm}^{-2}$  of  $\text{Si}^+$  ions with incident energies of 50 keV or 500 keV, and then a 10 nm thick boron layer was deposited onto the surface of the Si substrate. The samples were subsequently annealed at 900, 950 and 1010 °C for 15 s. Fig. 25 shows SIMS profiles of

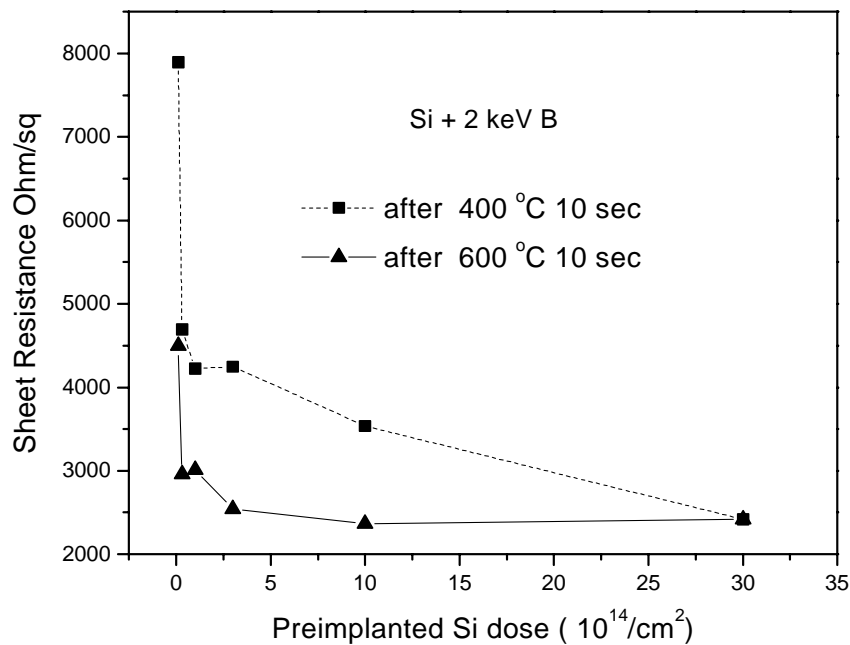


Fig. 24. Sheet resistance of samples annealed at low temperature with 500 keV Si co-implantation at different doses. Zero dose represents control samples [125].

boron after annealing at 950 °C for 15 s. 500 keV implanted sample exhibits more B diffusion retardation than the 50 keV implanted. Fig. 26 shows the penetration depths of B diffusion under other annealing conditions. If we define diffusion as “suppressed” or “enhanced” by comparing diffusion profiles in virgin Si after the same annealing process, then we have suppressed diffusion in 500 keV or 50 keV  $\text{Si}^+$  irradiated Si after 900 °C, 15 s or 950 °C, 15 s annealing, but enhanced diffusion occurred in the 50 keV-irradiated sample after annealing of 1010 °C 15 s. The different diffusion behaviors for

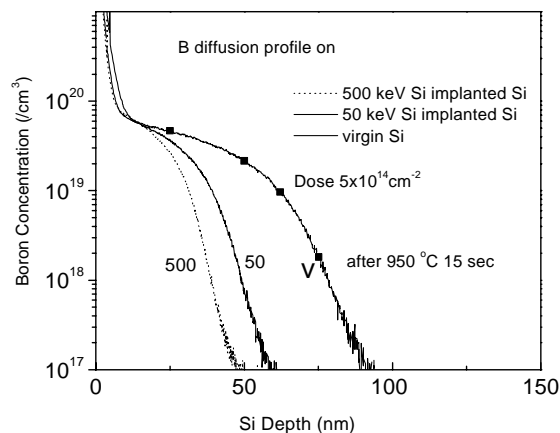


Fig. 25. SIMS profiles of boron diffused from a surface layer deposited onto an ion implantation damaged substrate. The samples were first implanted with  $5 \times 10^{14} \text{ cm}^{-2}$  of Si ions having incident energies of 50 keV or 500 keV, and then a 10 nm thick layer of boron layer was deposited onto the Si substrate. The samples were subsequently annealed at 950 °C for 15 s [112].

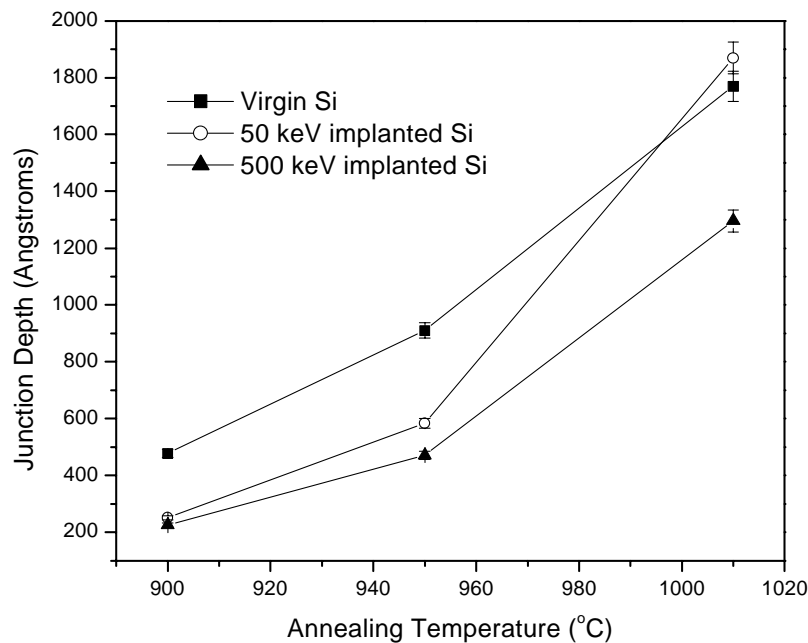


Fig. 26. Penetration depth of B extracted from SIMS profiles after annealing at 900, 950 and 1050 °C for 10 s. Samples were implanted with  $5 \times 10^{14} \text{ cm}^{-2}$  50 keV or 500 keV Si ions prior to B deposition.

50 keV and 500 keV-irradiated samples can be explained as follows: (1) surface vacancy rich regions created by implantation will provide excess vacancies to recombine with the interstitials responsible for BED. Suppressed B diffusion is expected due to a decreased population of Si interstitials. (2) It is easier for the interstitial B atoms to occupy a substitutional site via the reaction  $B_i + V \rightarrow B_s$ . (3) End of range defects can also behave as a sink for Si interstitials that would contribute to boron-enhanced diffusion. When the annealing temperature goes up to 1010 °C, EOR defects in 50 keV-irradiated samples begin to dissolve, and large amounts of interstitials emitted from EOR defects will contribute to boron enhanced diffusion. EOR defects in 500 keV-irradiated samples are difficult to anneal out due to their deeper location. B diffusion is suppressed for a longer time, until the EOR defects are annealed out.

Rutherford back-scattering spectrometry (RBS) and channeling measurements were carried out with 2.0 MeV and 3.05 MeV  $\text{He}^+$  ions to obtain damage profiles. Fig. 27(a) shows RBS random and channeling profiles of the samples implanted with  $5 \times 10^{14} \text{ cm}^{-2}$  dose of 50 keV Si, as implantation and after RTA. It can be seen that defects in the 50 keV Si implanted sample are annealed out after a 900 °C, 15 s annealing. RBS channeling profiles after a 1010 °C, 15 s annealing are close to that of the virgin sample. Conventional and high-resolution transmission electron microscopy were used to study cross-sections of the samples in the  $\langle 011 \rangle$  directions. Transmission electron microscopy confirms that most EOR defects are annealed out under such annealing conditions. Annealing of end of range dislocations produced with different implantation energies is obvious. More time will be needed for annealing out the defects in 500 keV implanted Si because they are more deeply located. It shows a large region with dislocation loops in a 500 keV Si irradiated sample even after 1010 °C, 15 s annealing (Fig. 27(b)). From transmission electron microscopy (Fig. 28), no residual defects are present to a depth of 700 nm below the surface in 500 keV Si implanted and annealed samples. However, at the depth from 700 to 850 nm, a band of dislocation loops remain. Note that the surface region is a B-doped region, yet RBS shows that this region is well crystallized after

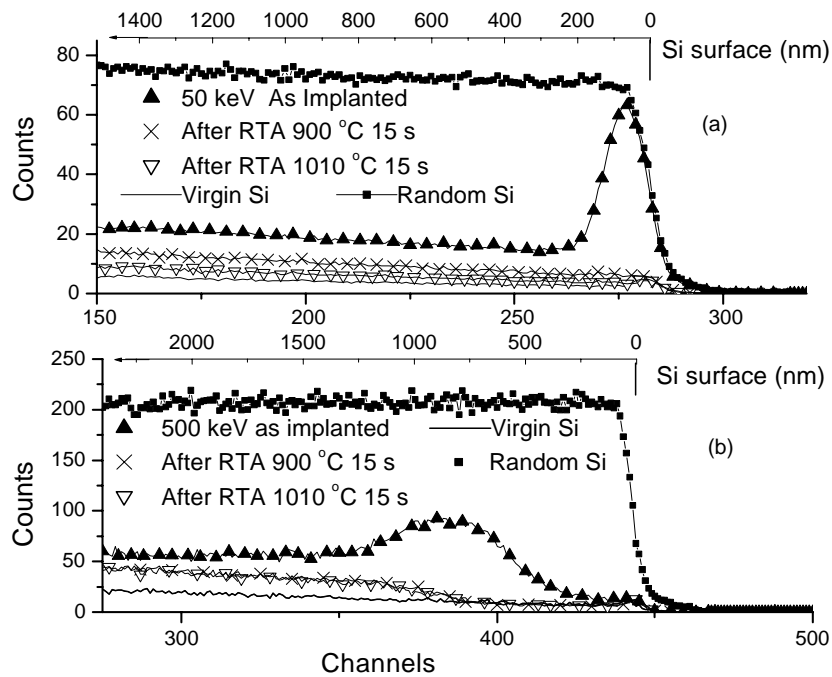


Fig. 27. RBS/channeling analysis of the Si sample irradiated with  $5 \times 10^{14} \text{ cm}^{-2}$  (a) 50 keV Si ions or (b) 500 keV Si ions and RBS profiles for these samples after 900 °C or 1010 °C 15 s RTA annealing. RBS analysis was performed with 2.0 MeV  $\text{He}^+$  in (a) and 3.05 MeV  $\text{He}^+$  in (b) [112].

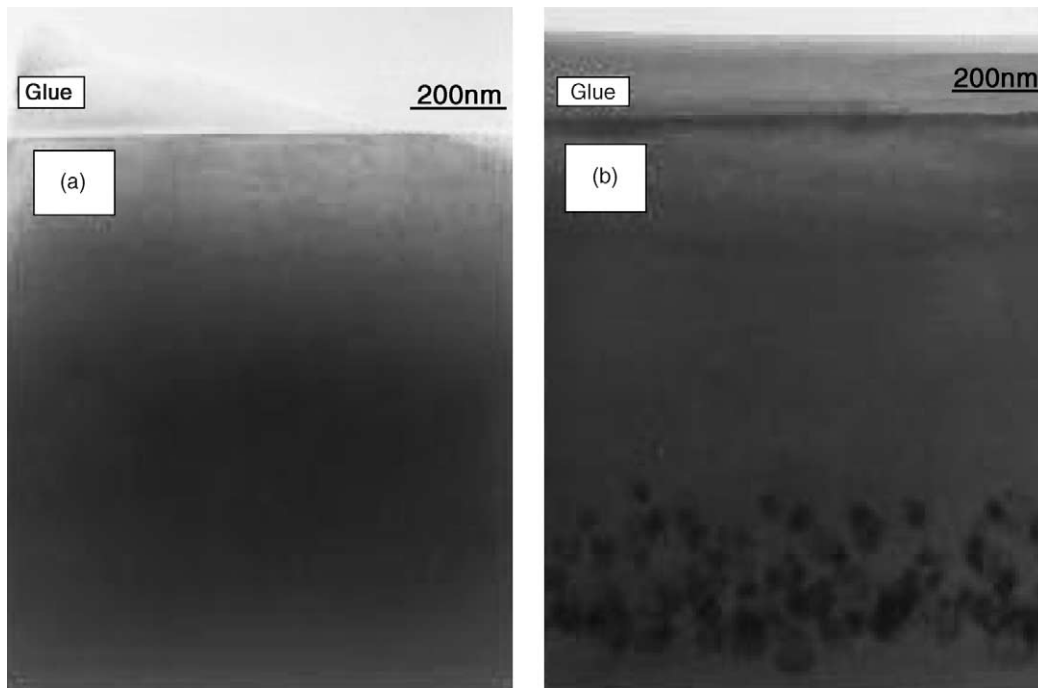


Fig. 28. Transmission electron microscopy images of (a) the Si sample irradiated with  $5 \times 10^{14} \text{ cm}^{-2}$  500 keV Si ions, and (b) same sample after RTA at 1010 °C for 15 s [112].

annealing. The device region is free from line defects and the defect region is far away from the surface.

### 5.7. Using PDE to increase stability of junctions

Spike annealing has become one of the most promising annealing techniques to satisfy the demand for the fabrication of CMOS devices with a gate length of less than 100 nm. Spike annealing process is to expose the samples at the peak temperature for little or no dwell time in order to minimize the anomalous diffusion of boron due to transient-enhanced diffusion and boron-enhanced diffusion. However, high-temperature annealing followed by quenching is a thermodynamically non-equilibrium process. Junctions formed by laser annealing have been shown to be intrinsically unstable [127]. The meaning of “being unstable” here is that junctions can not satisfy the device requirement after subsequent thermal process. For example, a junction may become much deeper or its resistivity is significantly increased. If spike annealing cannot anneal out the implantation damage completely or new interstitial sources are generated during spike annealing, interstitials injected will cause the dopants to redistribute and deepen the junction depth during subsequent thermal processes.

In a recent study by Shao et al. [128], an n-type Czochralski-grown Si (1 0 0) wafer was implanted at room temperature with boron ions at an energy of 0.2 keV to a dosage of  $1 \times 10^{15} \text{ cm}^{-2}$ . The sample was then cut into several pieces and annealed at 1100 °C for 1 s under flowing nitrogen gas. RTA was performed with a commercial rapid thermal processor HEATPULSE. A typical ramp-up rate is  $\sim 100 \text{ }^\circ\text{C/s}$ . After RTA, samples were then annealed at temperatures between 550 and 750 °C for stability studies.

Fig. 29 shows the SIMS profiles of boron in the Si samples after 1100 °C spike annealing and those after additional furnace annealing at 750 °C for 3 h. Anomalous diffusion was observed for the samples during post-spike furnace annealing. The instability is obvious, and is believed to be due to the perturbation by interstitials. A decreased density of interstitials will result in increased stability. The same authors [115] introduced MeV implantation to overcome instability by performing 1 MeV Si ion implantation to a dosage of  $1 \times 10^{16} \text{ cm}^{-2}$ . Fig. 29 shows the diffusion of B for MeV Si implanted sample is significantly reduced after subsequent furnace annealing at 750 °C for 3 h. Fig. 30 shows the dependence of diffusion length on the annealing temperature with respect to  $T = 700$  and 750 °C for annealing time  $t = 3$  h. With MeV implantation, B diffusion length upon additional furnace annealing was around 2 and 5 nm for 700 and 750 °C, respectively. These are comparable to the normal diffusion length of 1 and 4 nm calculated from Fair’s diffusivities.

PDE can indeed increase the stability of junctions formed by other techniques such as laser annealing and MBE [129]. Additional profile spreading during subsequent annealing was significantly reduced. Fig. 31 shows the thermal stability of 15 nm B-doped junction after 10 min rapid thermal annealing at 800 °C under flowing nitrogen ambient. The junction was formed by MBE growth with a B concentration of around  $2 \times 10^{20} \text{ cm}^{-3}$ . MeV implanted sample has a significant diffusion reduction as a result of 800 °C anneals. Instability remains a key issue for device fabrication due to the necessary high-temperature post-growth steps, e.g. contact formation. Case in point,  $\text{TiSi}_2$ , predominant silicide used for interconnect to COMS devices needs a temperature higher than 750 °C to form low resistivity stable phase [130,131]. For highly doped layer the transformation temperature for desired phase was increased to around 850 °C [132]. In general cases, a junction able to remain stable above 700 °C is desired, and therefore, PDE serves hereby as an effective strategy to overcome the instability.

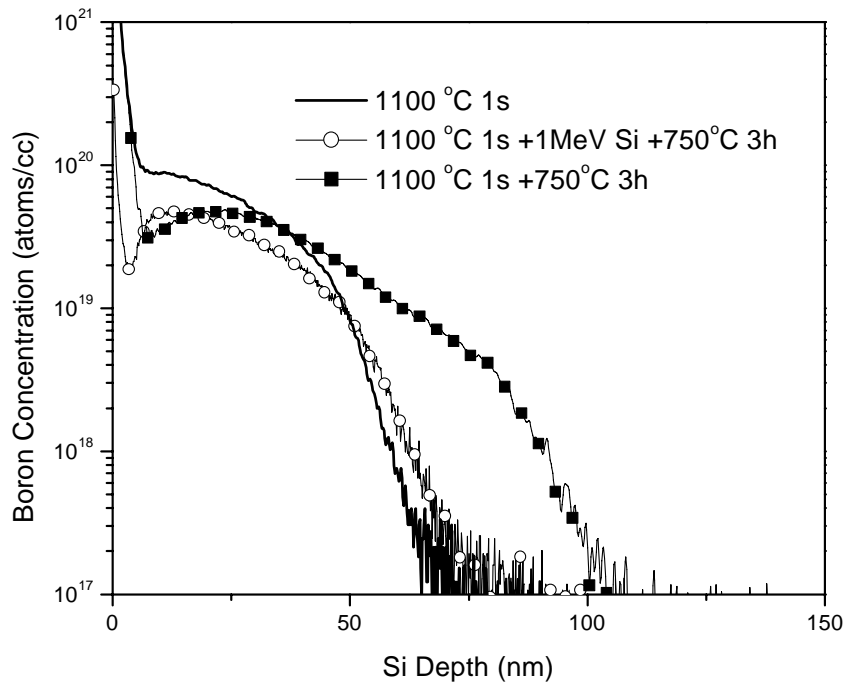


Fig. 29. SIMS profiles of boron in as-implanted and annealed samples. After 0.2 keV boron implantation, one-half of sample was spike annealed at  $1100^{\circ}\text{C}$  for 1 s, followed by furnace annealing at  $750^{\circ}\text{C}$  for 3 h. Another half sample was spike annealed at  $1100^{\circ}\text{C}$  for 1 s, followed by MeV Si implantation to a dosage of  $1 \times 10^{16} \text{ cm}^{-2}$ , then subsequently annealed at  $750^{\circ}\text{C}$  for 3 h. Anomalous diffusion is reduced by PDE [102].

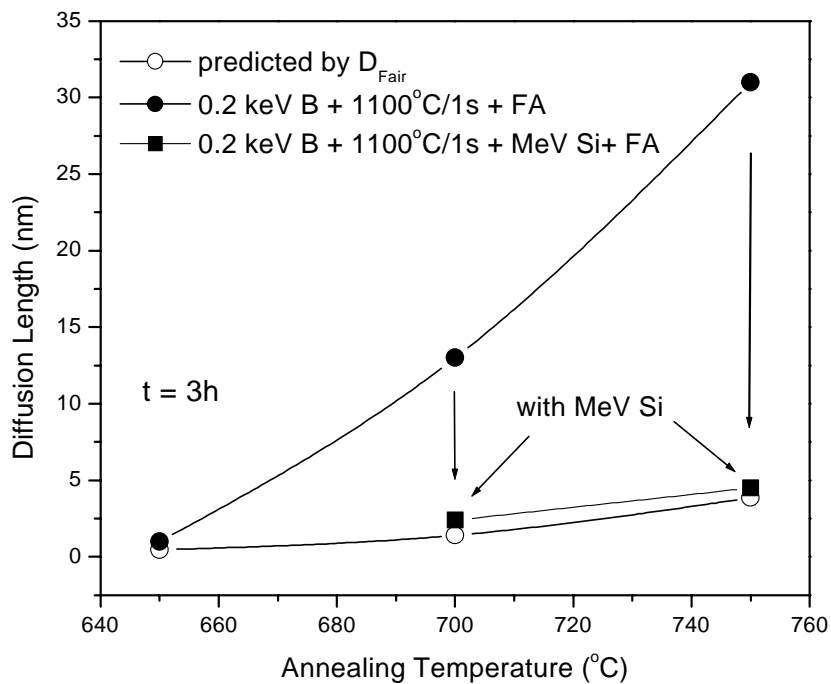


Fig. 30. Diffusion length of B extracted from SIMS profiles at annealing temperature  $750^{\circ}\text{C}$  (profiles given in Fig. 4) and at other annealing temperatures with or without MeV implantation inserted between spike annealing and furnace annealing [102].

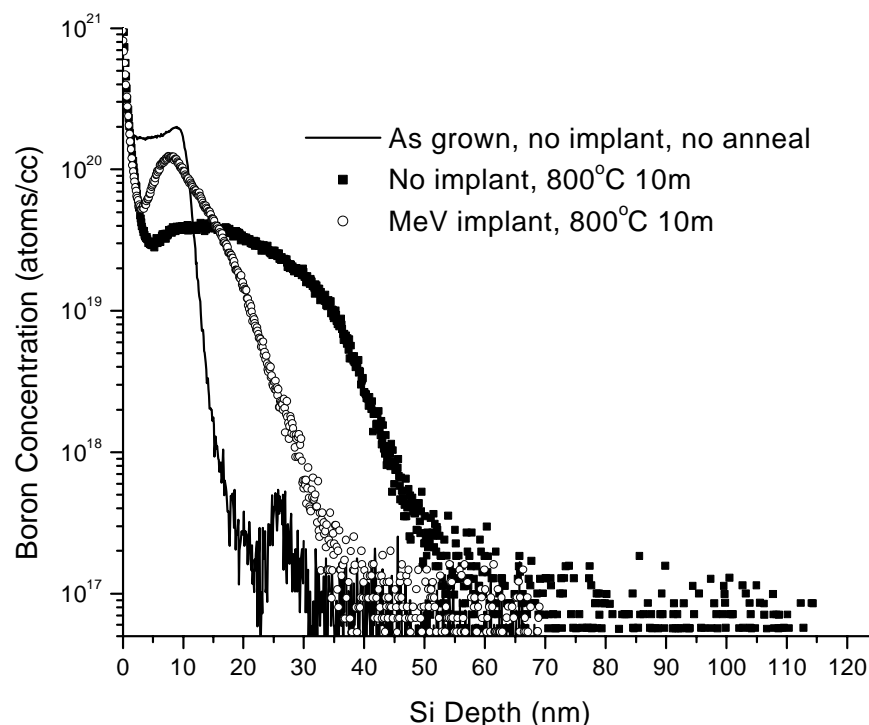


Fig. 31. SIMS B atomic concentration profiles of the 10 nm doped Si layer with or without  $5 \times 10^{15} \text{ cm}^{-2}$ , 1 MeV Si ion implantation, followed by 10 min annealing at 800 °C [129].

### 5.8. Retardation of oxygen enhanced diffusion

It is well known that oxidation of Si would produce a flux of interstitials from the interface of  $\text{SiO}_2$  and Si [2]. These interstitials can accelerate the diffusion of B in the bulk by kick-out reactions. This phenomenon was called oxygen enhanced diffusion. Retardation of oxygen enhanced diffusion of B in MeV implanted Si has been investigated [133]. This technique has been further developed as a method to detect vacancy clusters density, in which five B-doped layers were grown by molecular beam epitaxy, each with approximately  $4 \times 10^{19} \text{ cm}^{-3}$  peak concentration and separated by 100 nm of Si. There is a 100 nm capping layer above the spike closest to the surface and a buffer layer of 70 nm between substrate and the deepest spike. Samples were implanted with 1 MeV Si ions with a dose up to  $10^{16} \text{ cm}^{-2}$ , and annealed at 900 °C for 30 min under flowing oxygen. Each diffused spike after annealing was analyzed separately by comparing with non-diffused spike at corresponding depth, thus avoiding the errors due to slowly varying depth resolution during SIMS profiling. Fig. 32 shows the SIMS B depth profiles for these samples before and after annealing. The surface of these samples acts as an infinite source of interstitials due to the injection of interstitials during the growth of oxide [53]. Significant B diffusion was observed upon annealing and the spike close to the surface experienced more diffusion than those of the deeper layers. It is obvious that 1 MeV Si implantation was effective enough in inhibiting the B-diffusion and was even more so as the implantation dosage increases. Since the experimentally determined B diffusivity is proportional to the time average interstitial concentration  $C_I$ , The quantity  $C_I$  can be extracted from the profile spreading. Each SIMS profile in Fig. 32 represents a time-averaged profile of Si self-interstitials, which diffuses from a constant source into a substrate with a certain density of trapping centers.



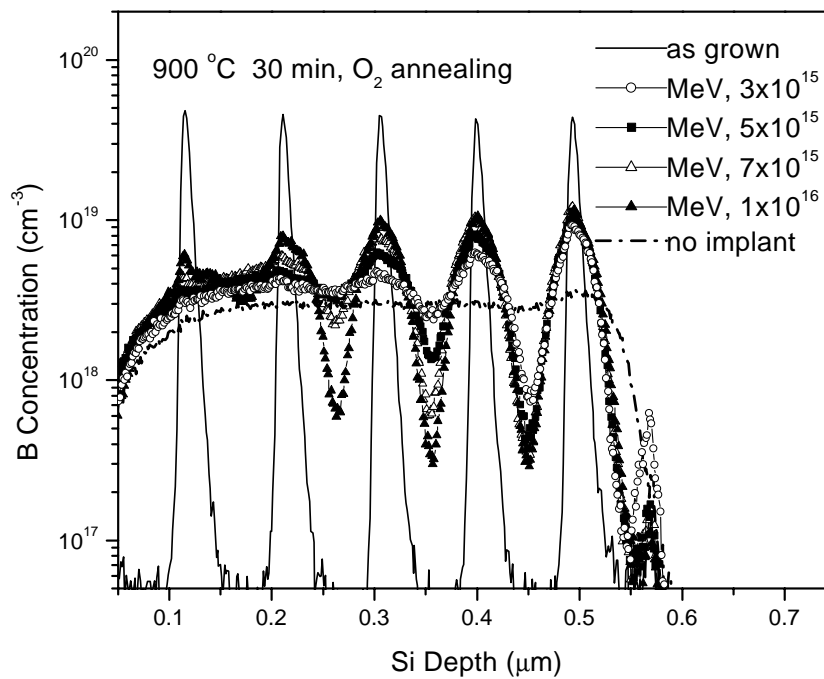


Fig. 32. Shows the SIMS measurement of B depth profiles for an as-deposited sample, and those implanted with 1 MeV Si ions at different dosages ranging from  $3 \times 10^{15}$  to  $10^{16} \text{ cm}^{-2}$  followed by annealing at  $900^\circ\text{C}$  for 30 min under flowing oxygen [133].

The calculated vacancy cluster densities indicate a non-linear relation with dosage for the 1 MeV implantation.

## 6. Other techniques to reduce B enhanced diffusion

### 6.1. Carbon co-implantation

The behavior of carbon in silicon has received more attention recently because of its influence on the formation of the extended defects and more importantly its influence on the diffusion of B in Si. The first reported surprising feature on the carbon implantation in Si is that no extended defects are formed after annealing. It was suggested that carbon getters through point defect or defect clusters [134]. Elimination of secondary defects and reduction of transient boron diffusion in preamorphized Si by C implantation was reported previously [135]. Efficiency of carbon in reduction of dislocation loop was only observed for high dosage C implantation [136]. It was also shown that only substitutional carbon is effective in suppressing the formation of extended defect while no such benefit is observed from non substitutional [137]. Aligned RBS show an enhanced damage accumulation in carbon implanted Si without post implantation annealing [138]. It was suggested that self-interstitial Si atoms are captured by the implanted C atoms, forming complex defects which are stable at room temperature [138]. A more detail study [139] indicated the formation of  $\text{Si}_{1.15}\text{C}$  complexes in annealed samples. They also show that once these complexes dissolve at annealing temperatures higher than  $900^\circ\text{C}$ , the effect of C is reduced and B transient

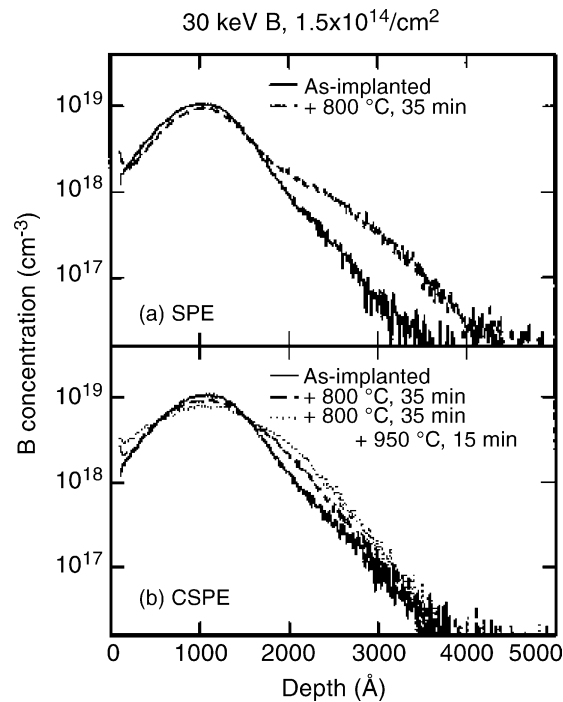


Fig. 33. SIMS measurement of B profiles after implantation ( $1.5 \times 10^{14} \text{ cm}^{-2}$ , 30 keV B) and after subsequent annealing. Sample in (b) refers to float zone wafers that were amorphized to a depth of 2  $\mu\text{m}$  by Si ion implantation, enriched with C by multiple implants to a level of  $5 \times 10^{18} \text{ cm}^{-3}$  over 1  $\mu\text{m}$ , and regrown at 500  $^{\circ}\text{C}$  for 1 h, 600  $^{\circ}\text{C}$  for 2 h, and 900  $^{\circ}\text{C}$  for 15 min. Sample in (a) was prepared as (b), but without the C implants [140].

diffusion is observed [139]. Fig. 33 shows the SIMS profiles of B before and after annealing at 800  $^{\circ}\text{C}$  for 35 min [140]. By incorporating substitutional C into B-doped Si using multiple C implantation followed by solid phase epitaxy, boron TED is fully suppressed for a doping level of C around  $5 \times 10^{18} \text{ cm}^{-3}$ , without perturbing electrical activity [140]. However, still there is concern that the C-related precipitates may cause junction leakage. These defects are hard to remove and may act as deep levels in Si [141].

Mechanism of carbon diffusion in silicon was first studied by Newman and Wakefield [142] and later by various groups [143–149]. Kalejs et al. [144] show that the out-diffusion of carbon is enhanced by the in-diffusion of phosphorus. This diffusion enhancement is suggested to be due to phosphorus-induced silicon self-interstitials and an appreciable diffusion component of carbon in silicon involving self-interstitials [144].

Assuming that carbon diffuses via the kick-out mechanism



the out-diffusion of grown-in C at high concentrations will lead to an undersaturation of I in the C-rich region. This undersaturation will reduce boron diffusion [145]. A recent extensive study has shown that I-trapping phenomenon involves very complex phenomena such as C clustering and C precipitation [148], formation of dicarbon-interstitial clusters and the boron–carbon-interstitial clusters [150], and formation of large carbon-interstitial clusters [151]. In one other recent study, Mirabella et al. placed a SiC layer between a deep B spike and surface TED source, whereby shunning the complexities due to carbon interaction with B and carbon out-diffusion.

They concluded that clustered C was no longer an interstitial trap and one self-interstitial deactivates two C traps [152].

## 6.2. Fluorine co-implantation

The implantation of  $\text{BF}_2^+$  molecular ions has been an important doping technique with obvious benefit of reduction of effective B implantation energy due to the mass ratio of boron to  $\text{BF}_2$ . Another benefit is the reduced B TED with improved short channel effects [153,154]. Shallow junction with low sheet resistance can be fabricated based on  $\text{BF}_2$  implantation with F preamorphization [154] or B implantation with F preamorphization [155]. F can also reduce P and As diffusion [156]. Introduction of F in source and drain extensions results in a better device performance with reduced leakage current [156]. It is, however, difficult to pinpoint the exact mechanism of fluorine effect due to B diffusion. Possible explanations can be trapping of Si interstitials by F [157], chemical bonding of F and B [158] or changed surface recombination rate of interstitials. It has been found that the presence of fluorine does not affect the evolution of dislocation loops in the end of range region [159].

Most recently, Mokheri et al. [158] have investigated the role of fluorine by using a buried B marker to monitor interstitial flux from the surface region, while wafers were preamorphized and implanted with either B, B + F,  $\text{BF}_2$ , As, As + F, or F. SIMS profiles in Fig. 34 show the retained fluorine dose after the RTA is highest in the boron-implanted samples. In all samples the buried layer has diffused by the same amount, indicating that there is no change to the silicon self-interstitials population due to fluorine. These results suggest that fluorine has a chemical effect and retards boron diffusion by mainly bonding with boron [158].

It has been reported that F atoms can segregate at  $\text{SiO}_2$ –Si interface and may also terminate the trivalent Si dangling bonds at the interface [160,161]. Strained Si–O–Si interface bonds may be replaced by Si–F and Si–O bonds [161]. This make the oxide vulnerable to B penetration and cause instability in the threshold voltage [162,163].

It is also reported that solid phase epitaxy growth (SPEG) of amorphized Si may form F bubbles [164,165]. The bubbles were distributed mostly near the original amorphous/crystalline interface and silicon surface where they deactivate surface B [165]. Furthermore, a damaged region near the

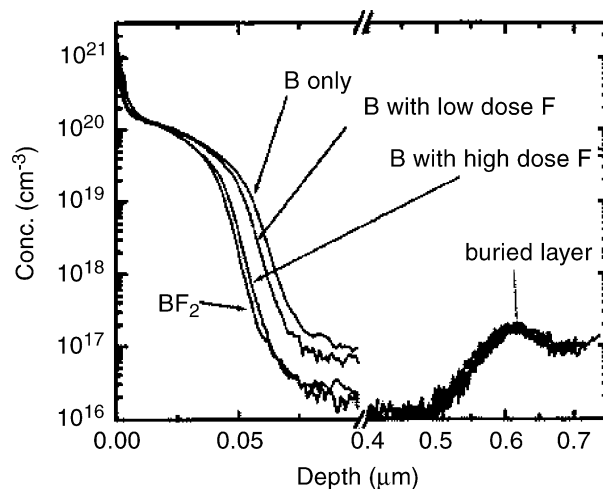


Fig. 34. SIMS profiles of B after annealing at 1050 °C. Boron diffusion is retarded by the presence of fluorine. Note that fluorine does not affect the diffusion of the buried boron layer [158].

crystalline-amorphous interface remains after recrystallization, and strong gettering of fluorine by this damage layer was observed [166]. However, with lower energy  $\text{BF}_2$  implant (2–5 keV) and 900 °C, 30 s annealing, no bubbles were detected and the majority of F evaporated [167].

### 6.3. Nitrogen bromine, chlorine, oxygen, selenium, sulfur, aluminum, gallium and indium co-implantation

Introduction of N into the gate or Si can effectively reduce the penetration of B through the gate oxides [168–170]. Reduction of B TED was also reported [171]. In explaining the effect of N on gate oxide integrity, it has been suggested that N may facilitate the recombination of Si interstitials and vacancies [170]. Another study by Chao et al. shows that formation of B–N complex may explain the retardation of boron diffusion [172]. A calculation by Li et al. has shown that a strong electronic bonding between B and N makes the migration energy of B much larger in Si [173].

Systematic studies on the effect of impurities on boron diffusion have been reported by Robertson et al. [174]. The impurities were implanted into and fully contained within the preamorphized Si. Diffusion and activation of B upon annealing was compared with control sample without co-implant of impurities. They conclude that:

- (a) Co-implantation bromine causes degradation of the electrical properties of the implanted boron. Co-implant has negligible effect on boron TED. Bromine implantation had no significant effect on the EOR defect evolution.
- (b) Co-implantation of chlorine reduces B TED but has no significant effect on the EOR defect evolution. However, it can reduce dopant loss.
- (c) Oxygen has no significant effect on the EOR defect evolution and increase boron diffusion significantly. Retained B exhibits lesser activation as compared to the control sample.
- (d) Selenium co-implantation causes extreme degradation in the electrical activation of B. Selenium has a negligible effect on B TED and has no significant effect on EOR defect evolution.
- (e) Sulfur co-implantation degrades the electrical activation of B and has no significant effect on the EOR defect evolution.

Li et al. [173] used an ab initio simulator to calculate the migration energy for B along the pathway where another species is present beside the channel. The simulation results are consistent with the experimental facts for a number of species (F, N, C, Al, Ga, In, Ge and B). The B migration energy can be changed by the strain effect from size misfit and by the electronic effect from the formation of bonding between the species and B. Calculated results show that the presence of F ( $E_m = 1.2$  eV), N ( $E_m = 0.97$  eV), C ( $E_m = 0.71$  eV), and Ge ( $E_m = 0.44$  eV) cause B  $E_m$  values to be larger than that with Si only ( $E_m = 0.33$  eV). Those results are consistent with experimental observations that the presence of all these species would decrease the B diffusion, whereas the presence of substitutional B beside the channel would accelerate B diffusion along the path way ( $E_m = 0.25$  eV). For F, aside from the argument of the reduction of Si-interstitials, the equilibrium B diffusivity itself is reduced by the fluorine incorporation. For N, the simulation result of high migration energy agrees with the experimental observation of formation of a B–N complex.

### 6.4. Preamorphization

Amorphization of Si by ion implantation and solid-state epitaxy is a well-studied topic. Many used preamorphization as a step toward reducing the channeling tail during dopant ion implantation [175]. Preamorphization by implantation of F, Si, Ar, Ge [176] and Sn [177] has been reported.

Dependence of boron diffusion on implantation temperature [178], annealing steps [179], amorphous depth [180,181] has been systematically studied. It was concluded that shallow junction can be produced by a combination of low temperature implants and two-step rapid thermal anneals [178,182–184].

Germanium is favorable for preamorphization since it produces a sharper amorphous and crystalline interface [185], exhibits fewer defects and lower leakage than those with Si or F [141]. Ge also has advantage of strain compensation. The larger Ge atoms can help balance the strain caused by the smaller B atoms [185]. It has been reported that boron diffusion has been reduced in preamorphized Si as compared to B TED in crystalline Si [176,179,186–189]. Pennycook et al. found no diffusion enhancement in preamorphized Si using the growth rate of boron containing precipitates as a criterion [187]. Özümk and Wortman showed that preamorphization of Si using Ge implantation could reduce, if not eliminate, any excess diffusion [188]. Sedgwick et al. [189] reported that pre- or postamorphized samples did not exhibit TED when the implanted B was confined within the preamorphized layer. It was suggested that interstitial-type dislocation loops found at crystalline–amorphous interface serves as a barrier to the transmission of the interstitials to the regrown crystal region where no diffusion enhancement occurs [189].

On the other hand, enhanced B diffusion with Si preamorphization has also been reported by a number of studies [71,190,191]. Wilson [192] reported a significantly larger anomalous diffusion in preamorphized Si as compared to the diffusion in crystalline Si after annealing. Cowern et al. [71] reported a nonequilibrium diffusion enhancement at a longer annealing time in preamorphized sample implanted with B at doses above the solid solubility limit, from which they speculated that some relatively slow-moving point defect complex created during the early stage of annealing might be the driving force for the enhanced diffusion. Guimarages et al. reported a greatly enhanced diffusion of B at high concentration with first a few seconds of electron beam annealing, but found no conclusive evidence for low B dosage. Enhancement was assumed to be caused by point defects remaining in the regrown layer which increased with boron concentration [193]. The study by Kim et al. [80] showed that rapid thermal annealing at 1150 °C resulted in an enhanced boron diffusion compared to that in single crystalline samples, though a reduced diffusion is observed in preamorphized samples annealed at 1000 °C. They interpreted this as due to the high efficiency of interstitial trapping by dense dislocation loops at 1000 °C annealing, and the fact that annealing at higher temperature of 1150 °C results in a small number of loops which can not effectively trap the interstitials. Most recently, Jones et al. have used B-doped superlattices to study TED in regrown Si. They concluded the existence of TED and also suggested that the controversy may be related to the different densities of the end of range loops, which determine the efficiency of loops as a barrier to interstitials [194].

Solmi et al. [190] and Servidori et al. [180] studied the diffusion of predeposited boron in postamorphized Si and showed the dependence of anomalous diffusion on the defect depth deposition. Diffusion was either enhanced or retarded, depending on whether the boron profiles were deeper or shallower than the depth of the post amorphized layer. Diffusion was correlated with dislocation loops at the end of range and with a vacancy-rich layer near the surface, which was produced by a post amorphization implant [190]. These authors use double-crystal X-ray diffraction and simulation methods to obtain the strain change caused by the defects. Si after regrowth showed a remarkable lattice contraction near the surface due to the vacancies, while interstitial type defects give rise to a lattice expansion with positive strain at the end of range of ions [180].

Preamorphization by 5 keV Ge implant can effectively reduce channeling of 1 and 2.5 keV B implants, but the benefit of preamorphization for sub-keV B is not obvious. As-implanted B profile

is almost undistinguishable for 0.2 keV B implants with or without preamorphization [195]. This may be due to the self amorphization of B in ultra-low energy region. On the other hand, preamorphized sample has a deeper profile of B after annealing. The benefits of preamorphization to reduce ion channeling are offset by the detrimental increase in TED and dopant segregations [195].

### 6.5. B diffusion in strained SiGe

Strained SiGe/Si heterostructures and superlattices are an essential component of many advanced Si-based devices. It has been found that B diffusivity in SiGe alloy can be reduced by an order of magnitude lower than that in Si [196]. The degree of B diffusion reduction increases with Ge fraction in the strained SiGe layers [197]. Moriya et al. explain this due to the change in the charged point defect concentration caused by band-gap narrowing [197]. This explanation is based on the critical assumption that B diffusion is mediated by the positively charged point defects. Another plausible explanation is the strain-dictated population of point defects [76]. This explanation gets the support from total-energy calculation [40] in which the authors computed the energies of formation for self-interstitials and vacancies in Si as a function of hydrostatic pressure. A linear increase in interstitial formation energy and decrease in vacancy formation energy were found with increasing pressure, corresponding to an outward relaxation of the lattice around the interstitial, and an inward relaxation of the vacancy [40]. Strain-induced changes in point defect formation energy has been experimentally investigated [76]. For a diffusing species in Si with

$$D_x = D_{(i)} + D_{(v)}, \quad (6.2)$$

where  $D_{(i)}$  and  $D_{(v)}$  are the interstitial and vacancy-mediated components of diffusion under strain-free conditions, the diffusivity was changed in a strained layer to

$$D_x = D_{(i)} \exp\left(-Q'_{(i)} \frac{s}{k_B T}\right) + D_{(v)} \exp\left(-Q'_{(v)} \frac{s}{k_B T}\right), \quad (6.3)$$

where  $s$  is the strain in the SiGe layer. Fitting to experimental data gives a value of  $Q'_{B(i)} = -17 \pm 3$  eV [76].

Diffusion of Sb in strained and relaxed Si and SiGe have been studied and Sb diffusivity is enhanced by compressive strain and retarded by tensile strain [198]. Experiments have confirmed the early prediction by Antonelli and Bernholc [40] and Cowern et al. [76], and suggested a vacancy-mediated mechanism for Sb diffusion in SiGe [199].

However, controversy still exists on the influence of strain. Kuo et al. showed that the diffusivity of B in  $\text{Si}_{1-x}\text{Ge}_x$  ( $x \leq 0.2$ ) was almost stress-independent [200]. The B diffusivity in nearly strain-free  $\text{Si}_{0.80}\text{Ge}_{0.20}$  is approximately equal to B diffusivity in fully strained  $\text{Si}_{0.80}\text{Ge}_{0.20}$ , which is about one order of magnitude lower than that in Si. The result indicates that boron diffusion in Si–Ge is predominantly a function of Ge content, rather than biaxial strain. The importance of Ge chemical content or microscopic strain has been suggested [200].

Further studies with  $x > 0.2$  meet challenges. It is difficult to grow thick and highly strained epilayers which do not undergo stress relaxation during diffusion measurements at elevated temperature [201]. Si–Ge superlattices are metastable and would relax to lower energy, less strained states on thermal annealing. Such relaxation may occur by the generation of misfit dislocation or by the interdiffusion of Si and Ge [202].



## 6.6. Multiple-step annealing

The technique of two-step annealing has been used to control dopant spreading, which is implemented as follows: (1) using first-step annealing at low temperature ( $\sim 500\text{--}600\text{ }^{\circ}\text{C}$ ) to do solid-phase epitaxial growth (SPEG); (2) using second-step annealing at a high temperature ( $800\text{--}1100\text{ }^{\circ}\text{C}$ ) to activate dopants and completely remove implantation damage. Previous studies showed that solid phase epitaxy growth, in combination with high-temperature annealing, resulted in essentially damage-free crystals based on Rutherford backscattering spectrometry channeling measurements [203–205]. The rate of SPEG depends on the type of dopant, dopant concentration, substrate orientation, and temperature. Temperature around  $550\text{ }^{\circ}\text{C}$  was the best condition to minimize the formation of end of range defects. A transmission electron microscopy study on arsenic ion implantation by Alessandrini et al. [182] showed that furnace annealing at  $550\text{ }^{\circ}\text{C}$ , in combination with high-temperature annealing at  $1000\text{ }^{\circ}\text{C}$ , produced the best epitaxial regrowth of Si with minimum defects. This result can be explained as what follows: (i) during the  $550\text{ }^{\circ}\text{C}$  first-step annealing, the amorphous Si regrows into a single crystal, and any imbalance of self-interstitials and vacancies are mostly annihilated, whereas dopant atoms remain mostly undiffused. (ii) During the  $1000\text{ }^{\circ}\text{C}$  rapid thermal annealing, the dopant will be activated with reduced interaction with Si interstitials because of the decreased density of defects. The two-step procedure, namely, first to remove defect then to activate dopants, can help reduce TED. Effect of diffusion suppression becomes more obvious for the case of amorphization. Significantly diffusion suppression has been reported for SiB, SiB<sub>2</sub>, and GeB<sup>−</sup> cluster ion implantation [183,184].

## 7. Evolution of vacancy and vacancy clusters in Si

### 7.1. Detection of vacancy

Vacancy is a fundamental defect which impacts PDE and has crucial effects on various properties of a host material. Techniques such as positron annihilation spectroscopy [206,207], X-ray strain measurements [208], and transmission electron microscopy have been used to detect the vacancy-type defects in the near surface region for high-energy implants. Quantitative estimate of excess vacancy-types defects has been realized by cross-section X-ray diffuse scattering [209]. More recently, Au labeling has also been used to obtain depth profiles of the vacancy-type defects [210], with the ability of quantification of those defects after calibration [211].

### 7.2. Evolution of vacancy clusters

Vacancy clusters are related to PDE in an obvious manner. The understanding about the vacancy clusters and their evolution is important in controlled PDE. Positron annihilation has emerged as an important tool that provides microscopic information on the vacancy defects which capture the positron and annihilate it through a localized electron. Granted, positron annihilation experiments in the past have indeed observed different lifetimes of positrons for mono-vacancies (270 ps) and di-vacancies (295–325 ps); yet the assignment of this longer lifetime is still full of controversy. Study on the stable structure of vacancy clusters using this method has reached its usefulness limits due to following two reasons:

- (1) Identification of cluster size needs theoretical modeling in assignment of various positron lifetimes, which is very much limited by the highly demanding analytical computing power.

Although a calculation of the lifetimes for multivacancies has been performed, the method is rather crude with electron density simply assumed to be a superposition of free-atom densities where geometry optimization is not carried out [212]. Not long ago, more accurate ab initio calculations have been performed for very small structure (mono- and di-vacancies) [213]. Using a small supercell with 38 atoms, the Hartree–Fock method has been applied to clusters with up to eight vacancies [214]. Due to the limitation of computing power, even the most aggressive calculation so far can only compute up to a size of 17 vacancies by treating a large supercell of 512 atoms [215].

- (2) Experimentally detected defect-related positron lifetimes and information thereby on the defect sizes typically have errors  $\sim 30$  ps for larger vacancy clusters. These errors are in the same range as the calculated lifetime differences between  $V_{10}$  and  $V_{14}$ , for example, hence posing a serious question on the reliability of positron lifetime calculations on which data analysis is based.

The simplest description of vacancy binding is achieved through a continuum binding model in which the topology of the cluster and its structural relation with the underlying lattice are neglected [216].  $E_b(n)$  is proportional to the change in the surface energy when a vacancy is added to an existing cluster:

$$E_b^c(n) = k_1 + k_2[n^{2/3} - (n-1)^{2/3}], \quad (7.1)$$

where  $k_1 = 3.65$  eV and  $k_2 = 5.15$  eV [217,218].

In an Ising-like binding model by counting of dangling bonds [219], binding energy can be expressed by

$$E = \sum_{\langle i,j \rangle} \frac{1}{2} E_b^1 S_i S_j, \quad (7.2)$$

where  $i$  and  $j$  represents the adjacent lattice sites. Calculation based on this model indicated that closed ring structures of vacancies, as they occur for  $V_6$  and  $V_{10}$ , should be especially stable [219]. Existence of magic sizes of vacancy clusters with  $n = 4m + 2$  (where  $m = 1, 2, 3, \dots$ ) was supported by total-energy calculations [220]. In theory, trigonal and planar ring hexavacancy ( $V_6$ ) are remarkably stable and essentially invisible to most electrical (deep-level transient spectroscopy) and optical [such as Fourier transform infrared absorption (FTIR)] methods of characterization [214], although they could be Raman active [214].

Most recently, an extended Ising model including the binding between vacancies located in second neighbor lattice sites has been put forth:

$$E = \sum_{\langle i,j \rangle} \frac{1}{2} E_b^1 S_i S_j + \sum_{\langle l,m \rangle} \frac{1}{2} E_b^2(S_k) S_l S_m, \quad (7.3)$$

where  $l$  and  $m$  are the second neighbor lattice sites, while  $k$  identifies the site between  $l$  and  $m$ . A kinetic Monte-Carlo simulation [221] based on this model showed that, rather than solely via free vacancies, the ripening of vacancy defects was also driven by the migration of small vacancy clusters, which produces faster vacancy agglomeration and more intense modification of cluster size distribution. Furthermore, in such calculations, a stable structure of  $V_{61}$  is expected, but the existence of such a larger vacancy clusters is not yet experimentally confirmed.



## 8. Conclusion

Transient-enhanced diffusion has been studied by various researchers for almost three decades. Only recently, the shrinking of microelectronics down to sub-micron size and demand on ultra-shallow junction have created an urgency to better understand the TED. The recognition of boron enhanced diffusion adds to an even more difficult problem which could be a roadblock to the progress in traditional CMOS fabrication. All anomalous diffusion of dopants in Si can be related to the deviation of Si point defect population from thermal equilibrium. Based on our studies and understanding, we propose to use point defect engineering to control diffusion. This review summarizes our understanding on B diffusion and our activities on the PDE. Retardation of B diffusion has been demonstrated such that ultra-shallow junction have been formed. However, integration issues, such as when to insert the high-energy ion implantation so as to minimize any adverse effects, must be addressed. Implementation of PDE on other structures such as SOI, SiGe are also underway. Eventually, advanced device concepts will most likely replace traditional MOS structures, but the timing for this revolutionary moment is still unpredictable. We are optimistic that PDE would be able to provide a bridge to the next step before the current technology has finally reached its ultimate limit.

## Acknowledgements

The authors would like to express their thanks to their collaborators in the PDE area: Phillip Thompson for providing MBE samples, Irene Rusakova for transmission electron microscopy studies, Paul van de Heide, Joe Bennett and Scott Baumann for SIMS analysis. We are grateful for the help of Xinming Lu, Xuemei Wang and Hui Chen for experiments and data analysis. The work was supported in part by the State of Texas through Advanced Technology Program and through the Texas Center for Superconductivity and Advanced Materials at the University of Houston. Part of reviewed results were from work supported by the MRSEC program of the National Science Foundation and by the Office of Naval Research. Portion of the work (Wei-Kan Chu) is also supported by his endowment from the Robert A. Welch Foundation.

## References

- [1] R.A. Swalin, *Atomic Diffusion in Semiconductors*, second ed., Wiley, New York, 1972.
- [2] P.M. Fahey, P.B. Griffin, J.D. Plummer, *Rev. Mod. Phys.* 61 (1989) 289.
- [3] M.M. de Souza, E.M. Sankara Narayanan, *Defect Diffusion Forum* 153–155 (1998) 69.
- [4] H. Zimmermann, *Defect Diffusion Forum* 153–155 (1998) 111.
- [5] H. Zimmermann, H. Ryssel, *Appl. Phys. A* 55 (1992) 121.
- [6] H. Bracht, N.A. Stolwijk, H. Mehrer, *Mater. Sci. Forum* 143–147 (1994) 785.
- [7] H. Bracht, N.A. Stolwijk, H. Mehrer, *Phys. Rev. B* 52 (1995) 16542.
- [8] T.Y. Tan, U. Gösele, *Appl. Phys. A* 37 (1985) 1.
- [9] F.F. Morehead, in: M. Stavola, S.J. Pearton, G. Davies (Eds.), *Defect in Electronic Materials*, Materials Research Society, Pittsburgh, 1988, p. 99.
- [10] W. Wijaranakula, *J. Appl. Phys.* 67 (1990) 7624.
- [11] K. Wada, N. Inoue, J. Osaka, in: by S. Mahajan, J.W. Corbett (Eds.), *Defect in Semiconductors II*, North-Holland, New York, 1983, p. 125.
- [12] K. Taniguchi, D.A. Antoniadis, Y. Matsushita, *Appl. Phys. Lett.* 42 (1983) 961.
- [13] A. Seeger, H. Föll, W. Frank, in: *Institute of Physics Conference Series* 31, N.B. Urli, J.W. Corbett (Eds.), *Radiation Effects in Semiconductors*, Institute of Physics, Bristol, 1977, p. 12.

- [14] M.R. Kump, R.W. Dutton, IEEE Trans. Comput. Aided Des. 7 (1988) 191.
- [15] H.U. Jäger, T. Feudel, S. Ulbricht, Phys. Status Solidi 116 (1989) 571.
- [16] G.B. Bronner, J.D. Plummer, J. Appl. Phys. 61 (1987) 5286.
- [17] C. Boit, F. Lau, R. Sittig, Appl. Phys. A 50 (1990) 197.
- [18] W. Wijaranakula, J. Electrochem. Soc. 139 (1992) 604.
- [19] K. Ghaderi, G. Hobler, M. Budil, L. Mader, H.J. Schulze, J. Appl. Phys. 77 (1995) 1320.
- [20] D. Maroudas, R.A. Brown, Phys. Rev. B 47 (1993) 15562.
- [21] R. Habu, A. Tomiura, Jpn. J. Appl. Phys. 35 (1996) 1.
- [22] S. Dannefaer, P. Mascher, D. Kerr, Phys. Rev. Lett. 56 (1986) 2195.
- [23] J.A. van Vechten, in: Proceedings of the March Meeting of the American Physical Society, New York City, Paper BI, 1987, p. 1 (unpublished).
- [24] H. Park, M.E. Law, J. Appl. Phys. 72 (1992) 3431.
- [25] D. Mathiot, J.C. Pfister, J. Appl. Phys. 55 (1984) 3518.
- [26] M. Jacob, P. Pichler, H. Ryssel, D. Gambaro, R. Falster, in: H.C. Graaff, H. van Kranenburg (Eds.), Proceedings of the 25th European Solid State Device Research Conference (ESSDER'95), Editions Frontieres, Gif sur Yvette, 1995, p. 203.
- [27] R. Car, P.J. Kelly, A. Oshiyama, S.T. Pantelides, Phys. Rev. Lett. 52 (1984) 1814.
- [28] P.J. Kelly, R. Car, Phys. Rev. B 45 (1992) 6543.
- [29] P.B. Rasband, P. Clancy, M.O. Thompson, J. Appl. Phys. 79 (1996) 8998.
- [30] P.E. Blöchl, E. Smargiassi, R. Car, D.B. Laks, W. Andreoni, S.T. Pantelidis, Phys. Rev. Lett. 70 (1993) 2435.
- [31] J. Zhu, T. Diaz de la Rubia, L.H. Yang, C. Mailhot, Phys. Rev. B 54 (1996) 4741.
- [32] P.J. Ungar, T. Halicioglu, W.A. Tiller, Phys. Rev. B 50 (1994) 7344.
- [33] I.P. Batra, F.F. Abraham, S. Ciraci, Phys. Rev. B 35 (1987) 9552.
- [34] M.M. de Souza, G.A.J. Amaratunga, in: S. Selberherr, H. Stippel, E. Strasser (Eds.), Simulation of Semiconductor Devices and Processes, vol. 5, Springer-Verlag, Berlin, 1993, p. 101.
- [35] M.I. Baskes, J.S. Nelson, A.F. Wright, Phys. Rev. B 40 (1989) 6085.
- [36] I. Kwon, R. Biswas, C.Z. Wang, K.M. Ho, C.M. Soukoulis, Phys. Rev. B 49 (1994) 7242.
- [37] C.Z. Wang, C.T. Chan, K.M. Ho, Phys. Rev. Lett. 66 (1991) 189.
- [38] G.A. Baraff, M. Schluter, Phys. Rev. B 30 (1984) 3460.
- [39] Y. Bar-Yam, J.D. Joannopoulos, Phys. Rev. B 30 (1984) 1844;  
Y. Bar-Yam, J.D. Joannopoulos, Phys. Rev. B 30 (1984) 2216.
- [40] A. Antonelli, J. Bernholc, Phys. Rev. B 40 (1989) 10643.
- [41] C.S. Nichols, C.G. Van de Walle, S.T. Pantelides, Phys. Rev. B 40 (1989) 5484.
- [42] J.L. Mercer Jr., M.Y. Chou, Phys. Rev. B 47 (1993) 9366.
- [43] G.H. Gilmer, T. Diaz de la Rubia, D.M. Stock, M. Jaraiz, Nucl. Instrum. Methods B 102 (1995) 247.
- [44] H.R. Schober, Phys. Rev. B 39 (1989) 13013.
- [45] M. Tang, L. Colombo, J. Zhu, T. Diaz de la Rubia, Phys. Rev. B 55 (1997) 14279.
- [46] K. Nishihira, T. Motooka, Phys. Rev. B 66 (2002) 233310.
- [47] R. Car, P. Blochl, E. Smargiassi, Mater. Sci. Forum 83–87 (1992) 433.
- [48] R. Virkkunen, M. Alatalo, M.J. Puska, R.M. Nieminen, Comput. Mater. Sci. 1 (1993) 151.
- [49] G.D. Watkins, in: S.T. Pantelides (Ed.), Deep Centres in Semiconductors, Gordon and Breach, New York, 1986.
- [50] P. Griffin, unpublished data (data obtained from P.J. Ungar, T. Halicioglu, W.A. Tiller, Phys. Rev. B 50 (1994) 7344).
- [51] R.A. Casali, H. Rucker, M. Methfessel, Appl. Phys. Lett. 78 (2001) 913.
- [52] Y. Okada, Phys. Rev. B 41 (1990) 10741.
- [53] S.M. Hu, J. Appl. Phys. 45 (1974) 1567.
- [54] R.F. Peart, Phys. Status Solidi 15 (1966) K119.
- [55] B.J. Masters, J.M. Fairfield, Appl. Phys. Lett. 8 (1966) 280.
- [56] J.M. Fairfield, B.J. Masters, J. Appl. Phys. 38 (1967) 3148.
- [57] H. Bracht, E.E. Haller, R. Clark-helps, Phys. Rev. Lett. 81 (1998) 393.
- [58] A. Ural, P.B. Griffin, J.D. Plummer, Phys. Rev. Lett. 83 (1999) 3454.
- [59] K.C. Pandey, Phys. Rev. Lett. 57 (1986) 2287.
- [60] K.C. Pandey, E. Kaxiras, Phys. Rev. Lett. 66 (1990) 915.
- [61] K. Compaan, Y. Haven, Trans. Faraday Soc. 52 (1956) 786.
- [62] K. Compaan, Y. Haven, Trans. Faraday Soc. 54 (1958) 1498.
- [63] S. Mantovani, F. Nava, C. Nobili, G. Ottaviani, Phys. Rev. B 33 (1986) 5536.
- [64] L. Kalinowski, R. Seguin, Appl. Phys. Lett. 35 (1979) 211.
- [65] L. Kalinowski, R. Seguin, Appl. Phys. Lett. 36 (1980) 171.
- [66] N.A. Stolwijk, B. Schuster, J. Hölzl, H. Mehrer, W. Frank, Physica Amsterdam 116B (1983) 335.
- [67] W.K. Hofker, H.W. Werner, D.P. Oosthoek, N.J. Koeman, Appl. Phys. 4 (1974) 125.
- [68] R.T. Hodgson, V.R. Deline, S. Mader, J.C. Gelpey, Appl. Phys. Lett. 44 (1984) 589.
- [69] R.B. Fair, J.J. Wortman, J. Liu, J. Electrochem. Soc. 131 (1984) 2387.

- [70] K. Cho, M. Numan, T.G. Finstad, W.-K. Chu, J. Liu, J.J. Wortman, *Appl. Phys. Lett.* 47 (1985) 1321.
- [71] N.E.B. Cowern, K.J. Yallup, D.J. Godfrey, D.G. Hasko, R.A. McMahon, H. Ahmed, W.M. Stobbs, D.S. McPhail, *Mater. Res. Soc. Proc.* 52 (1986) 65.
- [72] N.E.B. Cowern, D.J. Godfrey, D.E. Sykes, *Appl. Phys. Lett.* 49 (1986) 1711.
- [73] N.E.B. Cowern, K.T.F. Janssen, H.F.F. Jobs, *J. Appl. Phys.* 68 (1990) 6192.
- [74] N.E.B. Cowern, K.T.F. Janssen, G.F.A. van de Walle, D.J. Gravesteijn, *Phys. Rev. Lett.* 65 (1990) 2434.
- [75] N.E.B. Cowern, G.F.A. van de Walle, D.J. Gravesteijn, C.J. Vriezema, *Phys. Rev. Lett.* 67 (1991) 212.
- [76] N.E.B. Cowern, P.C. Zalm, P. van der Sluis, D.J. Gravesteijn, W.B. de Boer, *Phys. Rev. Lett.* 16 (1994) 2585.
- [77] N.E.B. Cowern, G. Mannino, P.A. Stolk, F. Roozeboom, H.G.A. Huizing, J.G.M. van Berkum, F. Cristiano, A. Claverie, M. Jarafz, *Phys. Rev. Lett.* 82 (1999) 4460.
- [78] A.E. Michel, W. Rausch, P.A. Ronsheim, R.H. Kastl, *Appl. Phys. Lett.* 50 (1987) 416.
- [79] A.E. Michel, M. Numan, W.-K. Chu, *Appl. Phys. Lett.* 53 (1988) 851.
- [80] Y.M. Kim, G.Q. Lo, D.L. Wong, H.H. Tseng, R. Hance, *Appl. Phys. Lett.* 55 (1989) 2316.
- [81] Y.M. Kim, G.Q. Lo, D.L. Wong, A.F. Tasch, S. Novak, *Appl. Phys. Lett.* 56 (1990) 1254.
- [82] D.J. Eaglesham, P.A. Stolk, H.J. Gossmann, J.M. Poate, *Appl. Phys. Lett.* 65 (1994) 2305.
- [83] P.A. Stolk, H.-J. Gossmann, D.J. Eaglesham, D.C. Jacobson, C.S. Rafferty, G.H. Gilmer, M. Jaraiz, J.M. Poate, H.S. Luftman, T.E. Haynes, *J. Appl. Phys.* 81 (1997) 6031.
- [84] S.C. Jain, W. Schoenmaker, R. Lindsay, P.A. Stolk, S. Decoutere, M. Willander, H.E. Maes, *J. Appl. Phys.* 91 (2002) 8919.
- [85] L.H. Zhang, K.S. Jones, P.H. Chi, D.S. Simons, *Appl. Phys. Lett.* 68 (1996) 499.
- [86] S.C. Jain, A.E. Hughes, *J. Mater. Sci.* 13 (1978) 1611.
- [87] M.D. Giles, *J. Electrochem. Soc.* 138 (1991) 1160.
- [88] A. Agarwal, T.E. Haynes, D.J. Eaglesham, H.-J. Gossmann, D.C. Jacobson, J.M. Poate, Y.E. Erokhin, *Appl. Phys. Lett.* 70 (1997) 3332.
- [89] B. de Mauduit, L. Laanab, C. bergaud, M.M. Faye, A. Martinez, A. Claverie, *Nucl. Instrum. Methods B* 84 (1994) 190.
- [90] A. Claverie, L.F. Giles, M. Omri, B. de Mauduit, G. Ben Assayag, D. Mathiot, *Nucl. Instrum. Methods B* 147 (1999) 1.
- [91] C. Bonafos, D. Mathiot, A. Claverie, *J. Appl. Phys.* 83 (1998) 3008.
- [92] C. Bonafos, M. Omri, B. de Mauduit, G. Ben Assayag, A. Claverie, D. Alquier, A. Martinez, D. Mathiot, *J. Appl. Phys.* 82 (1997) 2855.
- [93] R.B. Fair, G.A. Ruggles, *Solid-State Technol.* 33 (1990) 107.
- [94] L. Pelaz, M. Jaraiz, G.H. Gilmer, H.-J. Gossmann, C.S. Rafferty, D.J. Eaglesham, J.M. Poate, *Appl. Phys. Lett.* 70 (1997) 2285.
- [95] D.R. Lim, C.S. Rafferty, F.P. Klemens, *Appl. Phys. Lett.* 67 (1995) 2302.
- [96] M. Omri, C. Bonafos, A. Claverie, A. Nejim, F. Cristiano, D. Alquier, A. Martinez, N.E.B. Cowern, *Nucl. Instrum. Methods B* 120 (1996) 5.
- [97] A. Agarwal, H.-J. Gossmann, D.J. Eaglesham, L. Pelaz, D.C. Jacobson, T.E. Haynes, Y.U.E. Erokhin, *Appl. Phys. Lett.* 71 (1997) 3141.
- [98] A. Agarwal, H.-J. Gossmann, D.J. Eaglesham, S.B. Herner, A.T. Flory, T.E. Haynes, *Appl. Phys. Lett.* 74 (1999) 2435.
- [99] N.E.B. Cowern, M.J.J. Theunissen, F. Roozeboom, J.G.M. van Berkum, *Appl. Phys. Lett.* 75 (1999) 181.
- [100] A. Armigliato, D. Nobili, P. Ostojic, M. Servidori, S. Solmi, in: H.R. Huff, E. Sirtl (Eds.), *Semiconductor Silicon*, Electrochemical Society, New York, 1977.
- [101] S.T. Dunham, S. Chakravarthi, A. H. Gencer, *Tech. Dig. Int. Electron Devices Meet.* 501 (1998).
- [102] L. Shao, P.E. Thompson, P.A. van de heide, Q.Y. Chen, X.M. Wang, H. Chen, J. Liu, W.-K. Chu, *Phys. Rev. Lett.* Submitted for publication.
- [103] E. Napoltani, A. Carnera, E. Schroer, V. Privitera, F. Priolo, S. Moffatt, *Appl. Phys. Lett.* 75 (1999) 1869.
- [104] E. Napoltani, A. Carnera, V. Privitera, E. Schroer, G. Mannino, F. Priolo, S. Moffatt, *Mater. Res. Soc. Symp.* 610 (2001) B5.2.1.
- [105] K.B. Winterbon, *Radiat. Effects* 46 (1980) 181.
- [106] J. Biersack, L.G. Hagmark, *Nucl. Instrum. Methods Phys. Res. B* 174 (1980) 257.
- [107] V. Raineri, R.J. Schreutelkamp, F.W. Saris, K.T.F. Janssen, R.E. Kaim, *Appl. Phys. Lett.* 58 (1991) 922.
- [108] O.W. Holland, C.W. White, *Nucl. Instrum. Methods Res. B* 59–60 (1991) 353.
- [109] O.W. Holland, B. Nielson, D.S. Zhou, *J. Electron. Mater.* 25 (1996) 99.
- [110] V.C. Venezia, T.E. Haynes, A. Agarwal, L. Pelaz, H.-J. Gossmann, D.C. Jacobson, D.J. Eaglesham, *Appl. Phys. Lett.* 74 (1999) 1299.
- [111] L. Shao, X. Lu, J. Yue, Q. Li, J. Liu, P.A.W. Heide, W.-K. Chu, *Appl. Phys. Lett.* 74 (2000) 3953.
- [112] L. Shao, X. Lu, X. Wang, I. Rusokeva, J. Liu, W.-K. Chu, *Appl. Phys. Lett.* 76 (2001) 2321.
- [113] L. Shao, J.R. Liu, P.E. Thompson, X.M. Wang, H. Chen, W.-K. Chu, *Electrochem. Solid-State Lett.* 5 (2002) G93–G95.
- [114] L. Shao, P.E. Thompson, R.J. Bleiler, S. Baumann, X. Wang, H. Chen, J. Liu, W.-K. Chu, *J. Appl. Phys.* 92 (2002) 5793.

- [115] L. Shao, X.M. Wang, H. Chen, J. Liu, W.-K. Chu, *Electrochem. Solid-State Lett.* 6 (6) (2003) G82.
- [116] N.E.B. Cowern, *Appl. Phys. Lett.* 64 (1994) 2646.
- [117] G. Lulli, M. Bianconi, S. Solmi, E. Napolitani, A. Carnera, *J. Appl. Phys.* 87 (2000) 8461.
- [118] V.C. Venezia, L. Pelaz, H.-J.L. Gossmann, T.E. Haynes, C.S. Rafferty, *Appl. Phys. Lett.* 79 (2001) 1273.
- [119] T. Inada, A. Kuranouchi, H. Hirano, T. Nakamura, Y. Kiyota, T. Onai, *Appl. Phys. Lett.* 58 (1991) 1748.
- [120] Y. Kiyota, T. Nakamura, K. Muraki, T. Inada, *J. Electrochem. Soc.* 141 (1994) 2242.
- [121] S. Loududoss, S.L. Zhang, *Appl. Phys. Lett.* 64 (1994) 3467.
- [122] S. Saito, M. Kumagai, T. Kondo, *Appl. Phys. Lett.* 63 (1993) 197.
- [123] S. Saito, K. Hamada, A. Mineji, *Nucl. Instrum. Methods Phys. Res. B* 120 (1996) 37.
- [124] R. Murto, in: *Proceedings of the NIST Third National Implant Users Meeting*, Austin, TX, 21 October 1999.
- [125] L. Shao, X. Wang, J. Liu, J. Bennett, L. Larsen, W.-K. Chu, *J. Appl. Phys.* 92 (2002) 4307.
- [126] R. Kalyanaraman, V.C. Venezia, L. Pelaz, T.E. Haynes, H.-J.L. Gossmann, C.S. Rafferty, *Appl. Phys. Lett.* 82 (2003) 215.
- [127] W.-K. Chu, *Appl. Phys. Lett.* 36 (1980) 273.
- [128] L. Shao, X.M. Wang, I. Rusakova, H. Chen, J. Liu, J. Bennett, L. Larsen, J. Jin, P.A.W. van der Heide, W.-K. Chu, *J. Appl. Phys.* 92 (2002) 5788.
- [129] L. Shao, P.E. Thompson, J. Bennett, X.M. Wang, H. Chen, W.K. Chu, *Appl. Phys. Lett.* 83 (2003) 2823.
- [130] R.W. Mann, G.L. Miles, T.A. Knotts, D.W. Rakowski, L.A. Clevenger, J.M.E. Harper, F.M. D'Heurle, C. Cabral Jr., *Appl. Phys. Lett.* 67 (1995) 3729.
- [131] S.L. Zhang, C. Lavoie, C. Cabral Jr., J.M.E. Harper, F.M. d'Heurle, J. Jordan-Sweet, *J. Appl. Phys.* 85 (1999) 2617.
- [132] R. Beyers, D. Coulman, P. Merchant, *Appl. Phys. Lett.* 61 (1987) 5110.
- [133] L. Shao, unpublished.
- [134] H. Wong, N.W. Cheung, P.K. Chu, J. Liu, J.W. Mayer, *Appl. Phys. Lett.* 52 (1988) 1023.
- [135] S. Nishikawa, A. Tanaka, T. Yamaji, *Appl. Phys. Lett.* 60 (1992) 2270.
- [136] M. Tamura, T. Ando, K. Ohyu, *Nucl. Instrum. Methods B* 59 (1991) 572.
- [137] T.W. Simpson, R.D. Goldberg, I.V. Mitchell, *Appl. Phys. Lett.* 67 (1995) 2857.
- [138] J.P. de Souza, H. Boudinov, P.F.P. Fichtner, *Appl. Phys. Lett.* 64 (1994) 3596.
- [139] A. Cacciato, J.G.E. Klappe, N.E.B. Cowern, W. Vandervost, L.P. Biró, J.S. Custer, F.W. Saris, *J. Appl. Phys.* 79 (1996) 2314.
- [140] P.A. Stolk, D.J. Eaglesham, H.-J. Gossmann, J.M. Poate, *Appl. Phys. Lett.* 66 (1995) 1370.
- [141] E.C. Jones, E. Ishida, *Mater. Sci. Eng. R24* (1998) 1.
- [142] R.C. Newman, J. Wakefield, *J. Phys. Chem. Solids* 19 (1961) 230.
- [143] F. Rollert, N.A. Stolwijk, H. Mehrer, *Mater. Sci. Forum* 38–41 (1989) 753.
- [144] J.P. Kalejs, L.A. Ladd, U. Gosele, *Appl. Phys. Lett.* 45 (1984) 268.
- [145] R. Scholz, U. Gösele, J.-Y. Huh, T.Y. Tan, *Appl. Phys. Lett.* 72 (1998) 200.
- [146] R.F. Scholz, P. Werner, U. Gösele, T.Y. Tan, *Appl. Phys. Lett.* 74 (1999) 392.
- [147] H. Rückert, B. Heinemann, W. Röpke, G. Fischer, G. Lipper, H.J. Osten, R. Krups, in: *Proceedings of the International Conference on Simulation of Semiconductor Processes and Devices*, Cambridge, 1997.
- [148] H. Rückert, B. Heinemann, W. Röpke, R. Kurps, D. Krüger, G. Lippert, H.J. Osten, *Appl. Phys. Lett.* 73 (1998) 1682.
- [149] P. Werner, H.-J. Gossmann, D.C. Jacobson, U. Gösele, *Appl. Phys. Lett.* 73 (1998) 2465.
- [150] C.-L. Liu, W. Windl, L. Borucki, S. Lu, X. Liu, *Appl. Phys. Lett.* 80 (2002) 52.
- [151] R. Pinacho, P. Castrillo, M. Jaraiz, I. Martin-Bragado, J. Barbolla, H.-J. Gossmann, G.-H. Gilmer, J.-L. Benton, *J. Appl. Phys.* 92 (2002) 1582.
- [152] S. Mirabella, A. Coati, D. De Salvador, E. Napolitani, A. Mattoni, G. Bisognin, M. Berti, A. Carnera, A.V. Drigo, S. Scalese, S. Pulvirenti, A. Terrasi, F. Priolo, *Phys. Rev. B* 65 (2002) 45209.
- [153] K. Ohyu, T. Itoga, N. Matsuaki, *Jpn. J. Appl. Phys.* 29 (1990) 457.
- [154] S. Ando, H. Horie, M. Imai, K. Oikawa, H. Kato, H. Ishiwari, S. Hijiya, *IEEE Symp. VLSI Tech.* 65 (1990).
- [155] T.H. Huang, H. Kinoshita, D.L. Kwong, *Appl. Phys. Lett.* 65 (1994) 1829.
- [156] J. Kato, *J. Electrochem. Soc.* 137 (1990) 1918.
- [157] H.-H. Vuong, H.-J. Gossmann, C.S. Rafferty, H.S. Luftman, F.C. Unterwald, D.C. Jacobson, R.E. Ahrens, T. Boone, P.M. Zeitzoff, *J. Appl. Phys.* 77 (1995) 3056.
- [158] A. Mokhberi, R. Kasnavi, P.B. Griffin, J.D. Plummer, *Appl. Phys. Lett.* 80 (2002) 3530.
- [159] D.F. Downey, J.W. Chow, E. Ishida, K.S. Jones, *Appl. Phys. Lett.* 73 (1998) 1263.
- [160] Y. Ono, M. Tabe, Y. Sakakibara, *Appl. Phys. Lett.* 62 (1993) 375.
- [161] T.P. Ma, *Proc. Defect Engineering in Semiconductor Symposium*, San Francisco, CA, 26 April–1 May 1992, Material Research Society, Pittsburgh, 1992, p. 741.
- [162] J.R. Pfeister, F.K. Baker, T.C. Mele, H.-H. Tseng, P.J. Tobin, J.D. Hayden, J.W. Miler, C.D. Gunderson, L.C. Parrillo, *IEEE Trans. Electron. Devices* 37 (1990) 1842.
- [163] J.J. Sung, C.-Y. Lu, *IEEE Trans. Electron. Devices* 37 (1990) 2312.

- [164] S.P. Wong, M.C. Poon, H.L. Kwok, Y.W. Lam, J. Electrochem. Soc. 133 (1986) 2172.
- [165] C.W. Nieh, L.J. Chen, Appl. Phys. Lett. 48 (1986) 1528.
- [166] M.Y. Tsai, B.G. Streetman, P. Williams, C.A. Evans Jr., Appl. Phys. Lett. 32 (1978) 144.
- [167] S.B. Felch, B.S. Lee, D.F. Downey, Z. Zhan, R.J. Eddy, in: Proceedings of Ion Implantation Technology Conference, Austin, TX, 16–21 June 1996, IEEE, New York, 1997, p. 611.
- [168] B. Yu, D.-H. Ju, N. Kepler, C. Hu, IEEE Electron. Devices Lett. 18 (1997) 312.
- [169] C.T. Liu, Y. Ma, H. Luftman, S.J. Hillenius, IEEE Electron. Devices Lett. 18 (1997) 212.
- [170] W.V. Ammon, P. Dreier, W. Hensel, U. Lambert, L. Koester, Mater. Sci. Eng. B 36 (1996) 33.
- [171] T. Murakami, T. Kuroi, Y. Kawasaki, M. Inuishi, Y. Matsui, A. Yasuoka, Nucl. Instrum. Methods Phys. Res. B 121 (1997) 257.
- [172] T.S. Chao, M.C. Liaw, C.H. Chu, C.Y. Chang, C.H. Chien, C.P. Hao, T.F. Lei, Appl. Phys. Lett. 69 (1996) 1781.
- [173] H.-J. Li, P. Kohli, S. Ganguly, T.A. Kirichenko, S. Banerjee, P. Zeitoff, Appl. Phys. Lett. 77 (2002) 2683.
- [174] L.S. Robertson, R. Brindos, K.S. Jones, M.E. Law, D.F. Downey, S. Falk, J. Liu, Mat. Res. Soc. Symp. 610 (2001) B5.8.1.
- [175] B.L. Crowder, J.F. Ziegler, G.W. Cole, in: B.L. Crowder (Ed.), Ion Implantation in Semiconductor and Other Materials, Plenum Press, New York, 1973, p. 257.
- [176] T.D. Calder, H.M. Naguib, D. Houghton, F.R. Shepherd, Mater. Res. Soc. Symp. Proc. 35 (1984) 353.
- [177] M. Delfino, D.K. Sadana, A.E. Morgan, Appl. Phys. Lett. 49 (1986) 575.
- [178] P.K. Vasudev, A.E. Schmitz, G.L. Olson, Mater. Res. Soc. Symp. Proc. 35 (1984) 367.
- [179] C.I. Drowley, J. Adkisson, D. Peters, S.-Y. Chiang, Mater. Res. Soc. Symp. Proc. 35 (1984) 375.
- [180] M. Servidori, Z. Sourek, S. Solmi, J. Appl. Phys. 62 (1987) 1723.
- [181] A.C. Ajmera, G.A. Rozgonyi, R.B. Fair, Appl. Phys. Lett. 52 (1988) 813.
- [182] E.I. Alessandrini, W.-K. Chu, M.R. Poponiak, J. Vac. Sci. Technol. 16 (1979) 342.
- [183] X.M. Lu, L. Shao, J.R. Jin, Q. Li, I. Rusakova, Q.Y. Chen, J. Liu, P. Ling, W.-K. Chu, Mater. Res. Soc. Symp. Proc. 610 (2000) B4.5.
- [184] X.M. Lu, L. Shao, X. Wang, J. Liu, W.-K. Chu, J. Bennett, L. Larson, P. Ling, J. Vac. Sci. Technol. B 20 (2002) 992.
- [185] C.P. Wu, J.T. McGinn, L.R. Hewitt, J. Electron. Mater. 18 (1989) 721.
- [186] T.E. Seidel, IEEE Electron Device Lett. EDL-4, 353 (1983).
- [187] S.J. Pennycook, R.J. Culbertson, J. Narayan, J. Mater. Res. 1 (1986) 476.
- [188] M.C. Özürik, J.J. Wortman, Presented at Symposium on Rapid Thermal Processing at the Materials Research Society Spring Meeting, 21–23 April 1987, Anaheim, CA.
- [189] T.O. Sedgwick, A.E. Michel, V.R. Deline, S.A. Cohen, J.B. Lasky, J. Appl. Phys. 63 (1988) 1452.
- [190] S. Solmi, R. Angelucci, F. Cembali, M. Servidori, M. Anderle, Appl. Phys. Lett. 51 (1987) 331.
- [191] S. Solmi, F. Cembali, R. Fabbri, R. Lotti, M. Servidori, M. Anderle, R. Canteri, in: Proceedings of the Shanghai Workshop on Ion Implantation, Hangzhou, China, 2–3 June 1988.
- [192] R.G. Wilson, J. Appl. Phys. 54 (1983) 6879.
- [193] S. Guimarages, E. Landi, S. Solmi, Phys. Status Solidi A 95 (1986) 589.
- [194] K.S. Jones, R.G. Elliman, M.M. Petracic, P. Kringhøj, Appl. Phys. Lett. 68 (1996) 3111.
- [195] M.I. Current, M.A. Foad, A.J. Murrell, E.J.H. Collart, G. de Cock, D. Jennings, J. Vac. Sci. Technol. B 18 (2000) 468.
- [196] P. Kuo, J.L. Hoyt, J.F. Gibbons, J.E. Turner, R.D. Jacowitz, T.L. Kamins, Appl. Phys. Lett. 62 (1993) 612.
- [197] N. Moriya, L.C. Feldman, H.S. Luftman, C.A. King, J. Bevk, B. Freer, Phys. Rev. Lett. 71 (1993) 883.
- [198] P. Kringhøj, A.N. Larsen, S.Y. Shirayev, Phys. Rev. Lett. 76 (1996) 3372.
- [199] A.Y. Kuznetsov, J. Cardenas, D.C. Schmidt, B.G. Svensson, J.L. Hansen, A.N. Larsen, Phys. Rev. B 59 (1999) 7274.
- [200] P. Kuo, J.L. Hoyt, J.F. Gibbons, J.E. Turner, D. Lefforge, Appl. Phys. Lett. 66 (1995) 580.
- [201] J.W. Matthews, A.E. Blackeslee, J. Cryst. Growth 27 (1974) 118.
- [202] S.S. Lyer, F.K. LeGoues, J. Appl. Phys. 65 (1989) 4693.
- [203] L. Csepregi, W.-K. Chu, H. Mueller, J.W. Mayer, Radiat. Effects 28 (1976) 277.
- [204] L. Csepregi, E.F. Kennedy, T.J. Gallagher, J.W. Mayer, T.W. Sigmon, J. Appl. Phys. 48 (1977) 4234.
- [205] E.F. Kennedy, L. Csepregi, J.W. Mayer, T.W. Sigmon, J. Appl. Phys. 48 (1977) 4241.
- [206] B. Nielsen, O.W. Holland, T.C. Laung, K.G. Lynn, J. Appl. Phys. 74 (1993) 1636.
- [207] C. Szeles, B. Nielsen, P. Asoka-Kumar, K.G. Lynn, M. Anderle, T.P. Ma, G.W. Rubloff, J. Appl. Phys. 76 (1994) 3403.
- [208] S.L. Ellingboe, M.C. Ridgway, Nucl. Instrum. Methods Phys. Res. B 127–128 (1997) 90.
- [209] M. Yoon, B.C. Larson, J.Z. Tischler, T.E. Haynes, J.-S. Chung, G.E. Ice, P. Zschack, Appl. Phys. Lett. 75 (1999) 2791.
- [210] V.C. Venezia, D.J. Eaglesham, T.E. Haynes, A. Agarwal, D.C. Jacobson, H.J. Gossmann, F.H. Baumann, Appl. Phys. Lett. 73 (1998) 2980.
- [211] R. Kalyanaraman, T.E. Haynes, V.C. Venezia, D.C. Jacobson, H.-J. Gossmann, C.S. Rafferty, Appl. Phys. Lett. 76 (2000) 3379.
- [212] M.J. Puska, C. Corbel, Phys. Rev. B 38 (1988) 9874.

- [213] H. Seong, L.J. Chang, *Phys. Rev. B* 53 (1996) 9791.
- [214] J.L. Hastings, S.K. Estreicher, P.A. Fedders, *Phys. Rev. B* 56 (1997) 10215.
- [215] T.E.M. Staab, A. Sieck, M. Haugk, M.J. Puska, T.H. Frauenheim, H.S. Leipner, *Phys. Rev. B* 65 (2002) 115210.
- [216] M. Jaraiz, G.H. Gilmer, J.M. Poate, T. Diaz De LaRuia, *Appl. Phys. Lett.* 68 (1996) 409.
- [217] V. Raineri, M. Saggio, *Appl. Phys. Lett.* 71 (1998) 1673.
- [218] S.M. Myers, G.A. Petersen, C.H. Seager, *J. Appl. Phys.* 80 (1996) 3717.
- [219] D.J. Chadi, K.J. Lewis, *Phys. Rev. B* 38 (1988) 1523.
- [220] A. Oshiyama, M. Saito, O. Sugino, *Appl. Surf. Sci.* 85 (1995) 239.
- [221] A. La Magna, S. Coffa, L. Colombo, *Phys. Rev. Lett.* 82 (1999) 1720.